Analysis of Suspended Sediment Variability in a Large Highly Turbid Estuary Using a 5-Year-Long Remotely Sensed Data Archive at High Resolution

C. Normandin, B. Lubac, A. Sottolichio, F. Frappart, B. Ygorra, V. Marieu

HAL Id: insu-03678702

https://insu.hal.science/insu-03678702

Submitted on 25 May 2022

Key Points:
- Recurrent spatial patterns of suspended particulate matter are described, quantified, and statistically related to environmental forcing
- Local bathymetry strongly controls the spatial distribution of surface suspended particles in estuaries dominated by a turbidity maximum
- The maximum surface turbidity signals are identified to be statistically located on shoals regardless of environmental conditions

Correspondence to:
B. Lubac,
bertrand.lubac@u-bordeaux.fr

Analysis of Suspended Sediment Variability in a Large Highly Turbid Estuary Using a 5-Year-Long Remotely Sensed Data Archive at High Resolution

C. Normandin[1], B. Lubac[1] (ID), A. Sottolichio[1] (ID), F. Frappart[2] (ID), B. Ygorra[1], and V. Marieu[1] (ID)

[1]University of Bordeaux, EPOC, UMR 5805, Pessac, France, [2]LEGOS, University of Toulouse, CNES, CNRS, IRD, UPS. OMP, Toulouse, France

Abstract Spatial variability of surface suspended particulate matter (SPM) concentration in the Gironde estuary and their relationships with environmental forcing are investigated through high spatial resolution multispectral data collected from July 2013 to August 2018 by the Operational Land Imager (Landsat-8/OLI) and MultiSpectral Instrument (Sentinel-2/MSI). A principal component analysis using the T-mode orientation is applied to the discontinuous multiannual time series composed of 41 remotely sensed images. The three first principal components (PC1, PC2, and PC3) explain 65.7% of the total variance. The SPM distribution associated with PC1 and PC2 exhibits a privileged along-estuary direction of the oscillation modes, while the spatial patterns of PC3 are clearly dominated by lateral oscillations opposing channels and shoals. The main environmental factors affecting the SPM distribution are identified by the analysis of their temporal patterns. The tidal range and the daily river discharge control the spatial patterns of PC1 and PC2, while the tidal cycles and the wind speed are significantly correlated with PC3. Furthermore, the analysis in the along-estuary and lateral directions shows marked longitudinal and transverse SPM gradients and a strong control of bathymetry on the SPM spatial distribution. For the first time, we highlight that the maxima of surface residual turbidity are located on the shoals regardless of the environmental (tidal and hydrological) conditions. Compared to previous studies, usually based on single-point in-water column measurements, these results provide a novel and complementary description of the spatial variability of SPM. They are useful to validate sediment transport numerical models, but also may improve our understanding of suspended sediment dynamics in estuarine systems governed by an estuarine turbidity maximum.

Plain Language Summary Suspended sediments trapped in estuaries form a so-called estuarine turbidity maximum, which is of primary importance on many levels. By settling through the water column, suspended sediments induce bed sedimentation and changes in estuarine morphology. They also play a key role on water quality. They reduce the water transparency, limiting primary production, and eventually adsorb organic matter, bacteria, and pollutants. This study provides a statistical analysis of surficial suspended sediment concentration in the Gironde estuary, retrieved from 41 high resolution multispectral satellite images acquired between 2013 and 2018. For the first time, recurrent spatial patterns of suspended particles are described, quantified and statistically related to tidal range, daily river discharge, water depth, and wind speed. Results reveal the strong control of bathymetry on the surface concentration and show that maximum surface turbidity signals are located on shoals regardless of environmental conditions. Compared to previous studies, these results provide a novel and complementary description of the spatial variability of suspended particulate matter. Furthermore, they highlight that high resolution images are useful to validate sediment transport numerical models, but also improve understanding of suspended sediment dynamics in estuarine systems governed by an estuarine turbidity maximum.

1. Introduction

Morphodynamics, bio-geochemical cycles, and community ecology of estuaries and surrounding coastal environments are directly controlled by suspended sediment concentration and vertical sediment fluxes (Etcheber et al., 2007; Talke et al., 2009; Turner & Millward, 2002). Improving our understanding of fine sediment dynamics can be partly addressed by the characterization of the spatio-temporal distribution of the concentration of suspended particulate matter (SPM; Jay et al., 2015; Hudson et al., 2016), which are

the result of complex transport, deposition, and erosion processes (Dyer, 1988). However, the modes of variability of SPM show a high complexity, particularly in macrotidal systems dominated by estuarine turbidity maximum (ETM) zones. Their spatial and temporal components are associated with a large range of scales, from centimeters to kilometers and from second to years, respectively, which are related to the 3-D estuarine morphology (Grasso & Le Hir, 2019) and environmental forcing such as tide, river discharge, wind, and turbulence (Jalón-Rojas et al., 2017; Uncles et al., 2006). Observing and analyzing all the components of the SPM variability signal remain a major technical and methodological challenge (Jay et al., 2015).

The scientific literature allows to infer that at least two complementary observation systems are required to extensively record the spatio-temporal variability of SPM. Continuous long-term in situ monitoring programs provide high frequency data time series in a single- or multi-points of the estuary (Druine et al., 2018; Garel et al., 2009; Jalón-Rojas et al., 2015; Jalón-Rojas et al., 2016; Mitchell et al., 2012; Sottolichio et al., 2011). These data enable to investigate the variability of the turbidity over the different time scales using spectral decomposition techniques (French et al., 2008; Jalón-Rojas et al., 2017; Schoellhamer, 2002). However, extrapolation of results to the whole system is hazardous because of possible local effects related to the bathymetry (Ralston et al., 2012) and the difficulty to discriminate vertical mixing processes from horizontal advection (Hudson et al., 2016). Water color remote sensing missions provide long-term data time series at a lower time frequency (from few days to few weeks) but with a spatial coverage and resolution relevant to record the large range of spatial scales characteristic of estuarine environments (Gernez et al., 2015).

These last years, the ocean color data of the medium spatial resolution multispectral missions, Moderate Resolution Imaging Spectroradiometer (MODIS) and Medium-Resolution Imaging Spectrometer (MERIS), have been extensively used to analyze the variability of the surface SPM in turbid coastal environments, such as estuaries and deltas (Dogliotti et al., 2016; Doxaran et al., 2009; Feng et al., 2014; Hudson et al., 2016; Loisel et al., 2014; Shi et al., 2011). The statistical analyzes of the SPM variability were predominantly conducted from two main approaches. Climatological analyses based on a segmentation of the dataset by season or environmental forcing allow to characterize the average spatial distributions of SPM (Dogliotti et al., 2016; Hudson et al., 2016; Shi et al., 2011). The S-mode spectral decomposition identifies recurrent temporal patterns over space (Loisel et al., 2014) and quantify their statistical contribution to the total variance. These approaches mainly address the temporal variability of SPM but do not allow to statistically examine the main recurrent spatial patterns. Further, medium resolution data strongly limit the capability to investigate the spatio-temporal variability of SPM in the vicinity of bathymetric transition areas which play a major role on the distribution of sediment transport and trapping (Ralston et al., 2012). The launch in recent years of high spatial resolution sensors (HRS) on board Landsat-8 for the Operational Land Imager (OLI) and Sentinel-2 for the MultisSpectral Instrument (MSI) provide high-quality water color data (Pahlevan, Sarkar, et al., 2017; Pahlevan, Schott, et al., 2017; Zhu et al., 2019) relevant to analyze the SPM variability at small (O~10 m) to large (O~10^5 m) spatial scales (Caballero et al., 2018; Novoa et al., 2017; Qiu et al., 2016; Zhang et al., 2014).

The main objective of this study is to explore the high potential of HRS in order to statistically quantify the spatial variability of surface SPM in a complex estuarine environment. First, a principal component analysis using the T-mode orientation is carried out using a discontinuous multiannual time series composed of 41 OLI and MSI images collected from July 2013 to August 2018 in order to identify the main spatial patterns and to quantify the contribution of each environmental forcing. Then, a descriptive analysis of SPM is conducted to characterize main patterns of turbidity at decametric-to-kilometric scales.

2. Study Site

2.1. Physical Settings

The study site is the whole Gironde fluvio-estuarine system (FES), which is composed of the Gironde Estuary and the lower tidal portions of the Garonne and Dordogne rivers. Arbitrary limits have been chosen for this study, Bordeaux for the Garonne portion and Libourne for the Dordogne portion. The Gironde FES is located on the French Atlantic Coast (44°40′N to 45°40′N; 1°10′W to 0°0′E). It is the largest estuary of the Western Europe with a length of 75 km and a total surface of 635 km^2 (Figure 1a). The Gironde FES is a prototype of funnel-shaped system, where width increases exponentially in a seaward direction, from 3.2 km at the
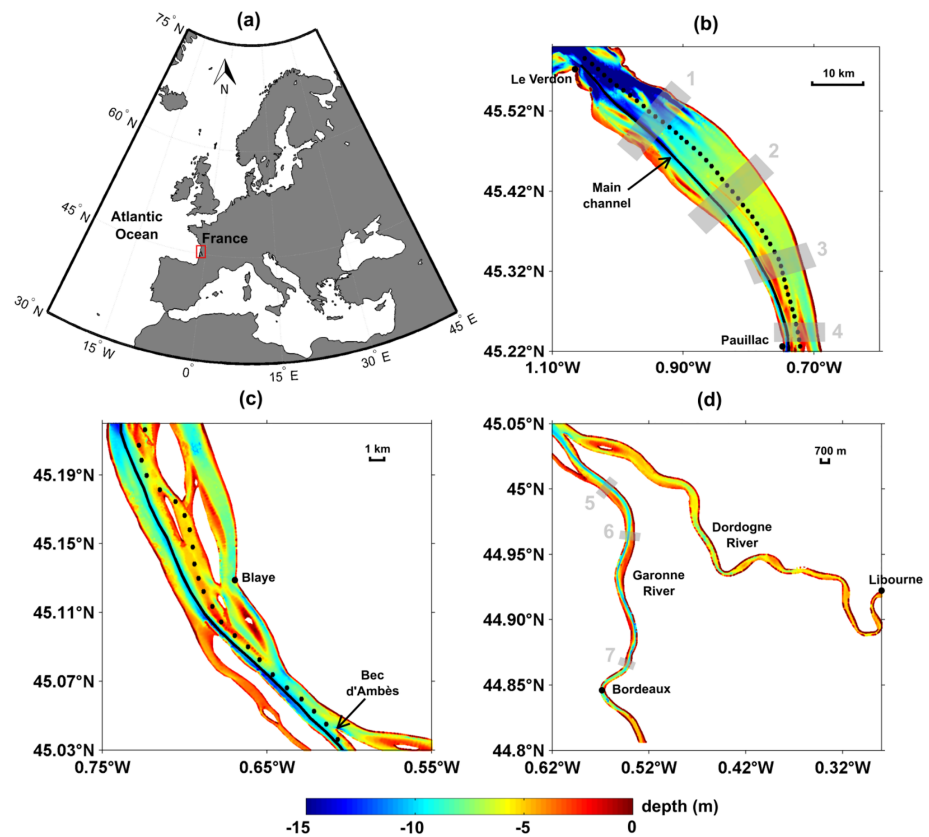
Figure 1. (a) Location of the Gironde fluvio-estuarine system (in the red box) and (b) bathymetry of lower area (from the mouth to Pauillac), (c) mid-reaches (from Pauillac to the confluence of the Garonne and Dordogne rivers, located at Bec d'Ambès), and (d) upper area (tidal portion of the Garonne and Dordogne rivers). The solid and dotted lines represent two longitudinal transects associated with the main channel and central shoal, respectively. The shaded boxes (from 1 to 7) represent different subareas used to generate average cross-sectional transects.

confluence between the Garonne and Dordogne rivers to 11 km in the lower reaches (Ross & Sottolichio, 2016).

Between 2000 and 2018, daily freshwater discharges were comprised between 50 and 2,500 m^3/s for the Garonne River and from 20 to 1,600 m^3/s for the Dordogne River, with the highest values in January to March and the smallest in August to September. (http://hydro.eaufrance.fr/). On average, 66% of the total freshwater inputs into the estuary are supplied by the Garonne River and 34% by the Dordogne River.

The morphology of the Gironde Estuary consists of a main (western) and secondary (eastern) channels separated by elongated sand bars and shoals in the lower area (Figure 1b) and by small islands in the mid-reaches of the estuary (Figure 1c). The western channel is used for navigation and has a mean depth of 9 m, artificially maintained by dredging, while the eastern channel has a depth of 7 m and evolves naturally. The depth can reach 20 m near the mouth (Sottolichio & Castaing, 1999). The morphology becomes simpler in the fluvial part of the system, featuring a broad channel and narrow shoals (Figure 1d).

In the Gironde FES, the tide is mainly semidiurnal with amplitudes ranging from 2.5 to 5 m at the mouth (Allen et al., 1974), classifying the estuary as macrotidal. The tide propagates up to the Garonne and the Dordogne Rivers along a distance of about 100 km upstream the confluence, before being completely damped by friction in both rivers. During its propagation along the estuary, the tide becomes asymmetric, and is characterized by a shorter flood and a longer ebb. For example, 4 hr and 8 hr 25 min are recorded for flood and ebb, respectively, in Bordeaux (Ross & Sottolichio, 2016). In addition, the tidal range increases regularly in the upstream direction. At spring tides, tidal range is about 5 m at the mouth and 6 m in Bordeaux, the maximum range being measured at 130 km from the mouth (Bonneton et al., 2015).

The aforementioned estuarine morphology and tide propagation are in permanent interaction. At the scale of the last 60 years, the general morphology has experienced continuous but weak trends of progressive infilling due to the natural siltation (Sottolichio et al., 2013). This lead to tidal amplification in the Dordogne and Garonne rivers, where the average tidal range increased for almost 80 cm between 1953 and 2014 (Jalón-Rojas et al., 2018). However, the main morphological features of the lower estuary (position of channels, banks and shoals) remained unchanged in the long term. At the scale of the 5 years covered by this study, the comparison of bathymetry charts and tidal records of 2013 and 2018 did not reveal any significant evolution. In particular, the tide curves and tidal range show same patterns in both years, meaning that tidal hydrodynamics did not change during this period.

2.2. Sediment Dynamics

In the Gironde FES, sediment dynamics are the result of the interaction between tides, river flow and morphology. A main feature is the existence of a highly concentrated ETM composed of silts and clays (Castaing et al., 1984), which motivates to focus this study in this specific system. Within the ETM, SPM concentrations often are over 1,000 g/m^3 in surface waters and can reach 10,000 g/m^3 near the bottom (Saari et al., 2010; Sottolichio et al., 2011). The main sources of fine sediment to the estuary are the watershed of the Garonne and the Dordogne rivers. They carry an average annual SPM flux comprised between 1.10^6 and 4.10^6 tons for the Garonne river, and less than $0.4.10^6$ tons for the Dordogne river (Coynel, 2005; Coynel et al., 2018).

In the estuary, river-derived SPM is submitted to erosion-deposition cycles driven mainly by tidal currents, at the scale of the semi-diurnal tidal cycle. This is the primary mechanism causing SPM variability in the water column. Asymmetry of the tidal wave induces the inequality between flood and ebb currents, leading to the well-known tidal pumping mechanism (Allen et al., 1980). This results on the trapping of mud in the estuary, which is recognized to be the main mechanism forming the ETM in the Gironde estuary (Allen et al., 1980; Sottolichio et al., 2000). The estuarine ETM follows seasonal shifts along the estuary (Allen et al., 1980), therefore its position varies through the year, with a total mass estimated to be comprised between 3.10^6 and 5.10^6 tons (Jouanneau & Latouche, 1981), which represent between 2 and 3 years of riverine inputs. Recent studies based on the analysis of continuous turbidity records at fixed stations in the Gironde estuary confirmed that in the ETM, average turbidity reaches 10 000 NTU, while under high river flow, the ETM is shifted away and turbidity values decrease to an order of magnitude between 10 and 1000 NTU (Jalón-Rojas et al., 2015, 2017). Therefore, it is assumed that most of the SPM signal in surface waters is the result of resuspension of estuarine trapped mud, and that the impact of river loads is minor to negligible in the short term.

Besides tidal currents, waves can play a significant role on the resuspension of mud in the shoals. However, in the Gironde estuary the effect of ocean waves is limited to the mouth. Wind-waves are likely to be effective in the narrow intertidal areas, but their effect is assumed to be local compared with the large scale of the estuary, and limited to the lower sections of the estuary.

The sediment distribution on the bed is relatively well known at the large scale of the estuary (Kapsimalis et al., 2004). It reflects the dominant sediment dynamics in the system and consists mainly of mud in the whole estuary, mixed with sand around the central banks and islands. At the mouth, the bed is exclusively sandy. In the rivers, the channel is composed of dominant sand and gravels but becomes muddy during low river flow periods, and the lateral flats are permanently muddy.

3. Data and Method

3.1. Water Color

OLI and MultiSpectral Instrument (MSI) products are sufficiently consistent for monitoring aquatic systems (Pahlevan et al., 2019). OLI and MSI data are used in this study to describe and quantify the spatial variability of SPM in relation with environmental parameters, at high resolution.

Landsat-8 satellite was launched on February 11th 2013 by the National Aeronautics and Space Administration (NASA). Lansat-8 joined former satellites to provide a continuous record of Earth's land surfaces since 1972 with Landsat-1. Its payload comprised the OLI and the Thermal Infrared Sensor (TIRS; Barsi et al., 2014). OLI operates in the visible, near-infrared (NIR) and shortwave infrared

Table 1
Characteristics of the Operational Land Imager (Landsat-8/OLI) and MultiSpectral Instrument (Sentinel-2/MSI)

Mission/Sensor		Landsat-8/OLI	Sentinel-2/MSI
Launch		February 2013	June 2015 (S2A)
			March 2017 (S2B)
Path time		10:45 (UT)	11:00 (UT)
Geometric revisit time		16 days	5 days with two satellites
			10 days with one satellite
Orbit		Sun-synchronous	Sun-synchronous
		Altitude 705 km	Altitude 786 km
Spectral bands	Deep blue	Band 1: 443 (26) nm – *30 m*	Band 1: 442 (45) nm – *60 m*
	Blue	Band 2: 483 (60) nm – *30 m*	Band 2: 492 (98) nm – *10 m*
	Green	Band 3: 561 (57) nm – *30 m*	Band 3: 559 (46) nm – *10 m*
	Red	Band 4: 655 (37) nm – *30 m*	Band 4: 665 (39) nm – *10 m*
	NIR	–	Band 5: 704 (20) nm – *20 m*
		–	Band 6: 739 (18) nm – *20 m*
		–	Band 7: 780 (28) nm – *20 m*
		–	Band 8: 833 (133) nm – *10 m*
		Band 5: 865 (28) nm – *30 m*	Band 8a: 864 (32) nm – *20 m*
		–	Band 9: 943 (27) nm – *60 m*
	Cirrus	Band 9: 1373 (21) nm – *30 m*	Band 10: 1377 (76) nm – *60 m*
	SWIR1	Band 6: 1609 (85) nm – *30 m*	Band 11: 1610 (141) nm – *20 m*
	SWIR2	Band 7: 2201 (187) nm – *30 m*	Band 12: 2186 (238) nm – *20 m*
Scene Size		170 km * 185 km	100 km * 100 km

(SWIR) in 9 spectral bands with a spatial resolution of 30 meters for multi spectral images and 15 m for panchromatic band. The Earth is fully observed every 16 days due to the Landsat-8′s orbit. The main characteristics of Landsat-8/OLI are given in Table 1. Orthorectified and terrain corrected Level 1T Landsat-8 were downloaded freely on https://earthexplorer.usgs.gov. Two tiles are necessary to cover the whole estuary. A total of 20 images have been downloaded with less than 10% of clouds between 2013 and August 2018.

Sentinel-2 is composed of two identical satellites 2A and 2B, which were launched on June 2015 and March 2017, respectively, by the European Space Agency (ESA). These two satellites provide the continuity of SPOT (Satellite Pour l'Observation de la Terre) and Landsat images for the Earth observations (Drusch et al., 2012). The two satellites are placed on the same orbit but phased at 180° (ESA website), allowing to acquire images every 5 days at the same location. The MSI is aboard and based on a push-broom concept. MSI acquires data in 13 spectral bands from visible to short-wave infrared wavelengths from 10 to 60 m spatial resolution. Detailed characteristics of Sentinel-2 are also given in Table 1. Sentinel-2 Level 1C products were downloaded freely from https://scihub.copernicus.eu/ using 3 tiles and 21 images have been downloaded with less than 10% of clouds between 2015 and August 2018.

In water color radiometry, biogeochemical parameters, such as SPM, are derived from the water leaving reflectance (ρ_w) signal (IOCCG, 2006). The accurate retrieval of the ρ_w product requires suitable atmospheric correction (AC) algorithms (IOCCG, 2010). In this study, Landsat-8/OLI L1T and Sentinel-2/MSI L1C images were processed using ACOLITE software version 20170718.0 (Vanhellemont & Ruddick, 2015), freely available online at http://odnature.naturalsciences.be/remsem/acolite-forum/, to obtain ρ_w. Although ACOLITE seems to show poor performance for very weakly turbid environments (Wei et al., 2018), we have selected this AC algorithm because it shows performance comparable to other algorithms for moderately turbid coastal and inland waters (Bru et al., 2017; Warren et al., 2019), and robust ρ_w retrievals for the Gironde estuary (Novoa et al., 2017). ACOLITE provides a large choice of atmospheric correction and aerosol epsilon options. In this study, the SWIR AC and full tile fixed epsilon options were selected as producing the best performance in moderately-to-highly turbid coastal waters such as the Gironde Estuary (Bru et al., 2017; Novoa et al., 2017; Vanhellemont & Ruddick, 2015). Cloud masking was performed using a reflectance threshold of 0.018 on the SWIR2 waveband. For the other options, the default setting was used. To conduct statistical analysis, OLI and MSI data are projected on the same 30x30 m grid.

Table 2
Values of A^ρ, B^ρ, and C^ρ Coefficients, Spectral Band Centers (λ_{red}), and Switching Thresholds ($R_{rs}(\lambda_{red})$) Associated With Nechad et al. (2010; Nechad10) and Han et al. (2016; Nechad10-L and Nechad10-H) Algorithms

SPM models	Sensor	λ_{red} (nm)	R_{rs} (λ_{red})	A^ρ	B^ρ	C^ρ
Nechad10	OLI	655	-	289.29	2.1	0.1686
	MSI	664	-	355.85	1.74	0.1728
Nechad10-L	OLI	655	≤ 0.03	346.353	0	0.5
	MSI	664	≤ 0.03	396.005	0	0.5
Nechad10-H	OLI	655	≥ 0.045	1,221.390	0	0.3329
	MSI	644	≥ 0.04	1,208.481	0	0.3375

Gironde Estuary waters are characterized as medium-to-highly turbid. Selection of an inverse algorithm allowing to reproduce the three-order-of-magnitude range of SPM is a critical point in order to avoid a methodological bias in the study of the SPM variability. Note that for brevity, SPM will refer to surface SPM in the following of the paper. A wide range of algorithms were developed to retrieve SPM from ρ_w or the remote sensing reflectance (R_{rs}). In this study, an original methodology, initially developed in Loisel et al. (2014), is used in order to select the most appropriate algorithm to process water color data in the Gironde FES, in the absence of control field data. The method is based on the analysis of the descriptive statistics of the SPM products generated by different algorithms, validated and widely used in the scientific literature, and on an inter-comparison exercise using scatter plots and mean relative difference maps. Three algorithms were selected: Nechad et al. (2010), noted Nechad10, Han et al. (2016), noted Han16, and Novoa et al. (2017), noted Novoa17. Nechad10 is commonly used (e.g., Caballero et al., 2018; Han et al., 2016; Novoa et al., 2017; Pahlevan et al., 2019) and can be considered as an historical semi-analytical algorithm. Han16 and Novoa17 are two multi-conditional algorithms based on switching criterion. They demonstrated a great improvement in the SPM retrieval performances for low-to-medium and highly turbid environments compared to previous approaches (Han et al., 2016; Novoa et al., 2017).

Nechad10 is a semi-analytical algorithm based on the well-known relationship between ρ_w and inherent optical properties in the red part of the spectrum (Nechad et al., 2010). This algorithm was developed using SPM values higher than 1.2 g/m^3 and lower than 110.3 g/m^3. As reported by Han et al. (2016), this medium SPM range can be considered as an inherent limitation of the algorithm in highly turbid waters. Nechad10 is based on the following equation:

$$\text{SPM} = A^\rho . \rho_w(\lambda_{\text{red}})/(1 - \rho_w(\lambda_{\text{red}})/C^\rho) + B^\rho \tag{1}$$

where λ_{red} is a spectral band in the red part of the spectrum, A^ρ (g/m^3) and C^ρ (dimensionless) are contants related to IOPs, and B^ρ (g/m^3) accounts for uncertainties in the measurements. Values of A^ρ, B^ρ, and C^ρ are given in Table 2.

Han16 is a multi-conditional approach based on a switching criteria using tuned versions of Nechad10. It was calibrated and validated from in situ SPM spanning about 4 orders of magnitude (from 0.15 to 2,626 g/m^3). This approach is based on two distinct tuned algorithms established for low-to-medium and high turbidity (Nechad10-L and Nechad10-H, respectively). A threshold value of R_{rs} in the red part of the spectrum is used as switching criteria. To avoid an artificial spatial pattern in the SPM distribution, a smoothing procedure is then applied. Following Han et al. (2016), the method consists in the definition of weighting functions for the low-medium (W_L) and high (W_H) SPM algorithms. Finally, SPM is computed as

$$\text{SPM} = \frac{W_L * \text{SPM}_L + W_H * \text{SPM}_H}{W_L + W_H} \tag{2}$$

where SPM_L and SPM_H are associated with the retrievals of Nechad10-L and Nechad10-H, respectively. Tuned-values of A^ρ, B^ρ, and C^ρ and switching thresholds associated with the two algorithms are given in Table 3. Because of the lack of near-infrared waveband around 750 nm for Landsat-8/OLI, it is important to note that, in this study, only the version of Nechad10-H, using R_{rs} in the red, is investigated.

Table 3
Values of Switching Thresholds ($\rho_w(\lambda_{red})$) Associated With the Novoa et al. (2017) Algorithms (Novoa17) for the Gironde Estuary

SPM models	ρ_{W} (λ_{red})	SPM range (g/m^3)
Novoa17-L	<0.007	<8.5
Smoothing procedure	[0.007, 0.016]	[8.5, 9.2]
Novoa17-M	[0.016, 0.08]	[9.2, 42.5]
Smoothing procedure	[0.08, 0.12]	[42.5, 180]
Novoa17-H	≥ 0.12	≥ 180

Note. Novoa17-L and Novoa17-M are linear models using R_{rs} in the green and red bands, respectively. Novoa17-H is a polynomial model using ρ_w in the NIR band.

Novoa17 is based on a multi-conditional empirical approach using switching criterion, as Han16, but specifically dedicated to the SPM estimation in the Gironde Estuary (Novoa et al., 2017). It was calibrated and validated using in situ SPM data acquired in the estuary and ranging from 2.6 to 1,579 g/m^3. This approach is based on three distinct algorithms established for low, medium, and high turbidity (Novoa17-L, Novoa17-M,

and Novoa17-H, respectively). Novoa17-L and Novoa17-M are linear models using ρ_w in the green and red bands, respectively. Novoa17-H is a polynomial model using ρ_w in the NIR band. A threshold value of ρ_w in the red part of the spectrum is used as a switching criteria. As for Han16, a smoothing procedure is then applied. Reader can refer to Novoa et al. (2017) for equations of the models. In Table 3, the threshold values are given associated with the different models and the SPM ranges. Further, since there are no significant difference between the representative wavelengths of OLI and MSI bands, the default algorithm coefficients used in Novoa17 were applied for MSI data.

3.2. Environmental Data

To characterize the relationship between environmental forcing and spatial variability of turbidity in the Gironde Estuary, data on water levels, daily river discharges, wind direction and speed, were used from 2013–2001 to 2018–2008. Water heights, provided by the Port of Bordeaux, were continuously recorded every 1 minute at nine tidal gauge stations, located between Le Verdon and Bordeaux (see locations in Ross & Sottolichio, 2016). Because water height is time and space-dependent, we use the averaged tidal value over a period of ± 5 min centered around the time of acquisition of images. Then, average values were extrapolated for the whole estuary by linear interpolation of tidal gauge data on the same 30x30 m grid as for Landsat-8/OLI and Sentinel-2/MSI images. The interpolation is possible because the tide propagates along the estuary without phase lag or amplification between the left and right banks (Ross & Sottolichio, 2016) and because conditions for the formation of a tidal bore are not met in this portion of the estuary (Bonneton et al., 2015). Two additional variables were extracted from tidal records and used as proxy for tidal currents: (i) tidal range was computed as the difference between the high and low water levels and (ii) tidal stages (i.e. high tide, low tide, ebb and flood) were associated with the acquisition time of satellite images. These two variables indicate, at the first order, the intensity of tidal currents and mixing, which are the main driver of surface turbidity. The tidal range is an indicator at the scale of the fortnightly tidal cycles and the tidal stage is an indicator at the scale of the semi-diurnal tidal cycle, respectively. Daily river discharges were measured at Tonneins for the Garonne River and Pessac-sur-Dordogne for the Dordogne River. These daily in situ stations records are made available by the Banque Hydro (http://www.hydro.eaufrance.fr/), a French database from the Ministry of Ecology, Sustainable Development and Energy. Wind speed and direction came from two in situ stations located at Pauillac and Bordeaux-Mérignac. These stations are operated by the official service of meteorology and climatology in France (Météo France). Wind speed and wind direction are measured every hour at 10 m over the ground. For the statistical analysis, we used the averaged values over a period of ± 2 h centered around the time of acquisition of images. Finally, the environmental dataset is complemented by the open data bathymetry product distributed by the SHOM (Service d'Hydrologie et d'Océanographie de la Marine) at a resolution of 0.0002° (~20 m). Bathymetry data of the lower and upper areas are available in SHOM (2016a) and SHOM (2016b), respectively. As stated previously, the morphology of the estuary remained unchanged between 2013 and 2018 and therefore the bathymetry can be considered as representative of the whole period of observation.

3.3. Statistical Data Processing

Identification of spatial and temporal patterns of a single field can be conducted from spectral decomposition techniques (Bierman et al., 2011; Blondeau-Patissier et al., 2014; Vantrepotte et al., 2011). In this study, we select a Principal Component Analysis (PCA) using the T-mode orientation. In this case, statistical variables are samples in time and statistical observations are samples in space (Machado-Machado et al., 2011; Neeti & Eastman, 2014). This technique allows to process uncontinuous time series of images and to find the dominant recurring spatial patterns over time (Machado-Machado et al., 2011; Neeti & Eastman, 2014). The first components of PCA, which explained the maximum of variance, are spatial patterns. The loadings, which are the correlations between components and statistical variables, are temporal patterns. Data are organized in an $m{\times}n$ matrix, with m (= 550,000), the total number of points or 30x30 m pixels used for the mapping of the Gironde FES, and n (= 41), the number of maps. Before performing PCA, variables are centered and standardized in order to reduce sensitivity of the variance-covariance matrix to scaling. Finally, control of environmental variables on the spatial variability of SPM is investigated through a correlation analysis between loadings and environmental variables.
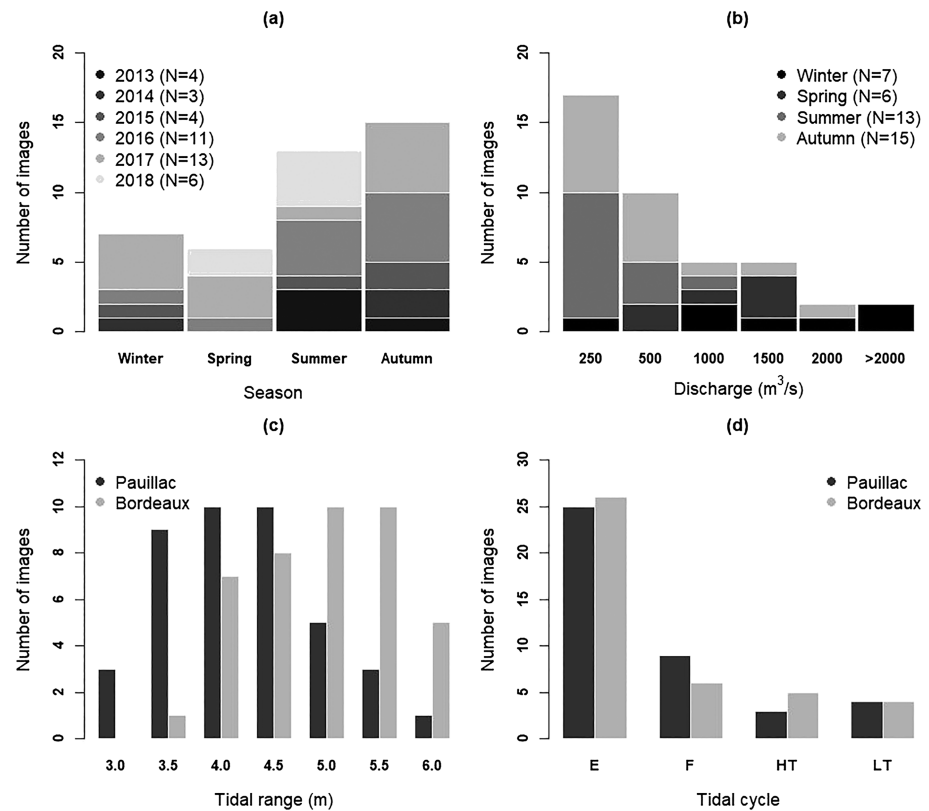
Figure 2. (a) Landsat-8/OLI and Sentinel-2/MSI images distribution per months and per classes of (b) daily river discharges (m³/s), (c) tidal range (m), and (d) tidal phase (E: ebb, F: flood, HT: high tide, LT low tide).

4. Results

4.1. Description of Environmental Forcing Context

High-quality Landsat-8/OLI and Sentinel-2/MSI images are not equally distributed over years and seasons (Figure 2a). The number of images available per year depends mainly on the number of operational space missions (see Table 1 for launch date), while the number of images per season is controlled by the atmospheric optical conditions. Summer (July –September) and fall (October–December) months ($N = 28$) are over-represented compared to winter (January–March) and spring (April–June) months ($N = 13$). This seasonal heterogeneity was expected since there are statistically more cloud-free observations in summer and the contribution of absorbing aerosols is minimum in fall (Bru et al., 2017).

Descriptive statistics of environmental conditions prevailing during the acquisition of satellite images are provided in Table 4. Daily river discharge is function of the season. Observations are directly impacted by

Table 4
Descriptive Statistics (Mean, Median, SD Standard Deviation, N: Number of Observations) of Daily River Discharge (m³/s) and Tidal Range (m) Computed for the Whole Dataset and Per Season

	River discharge (m³/s)			Tidal Range (m)-Pauillac			Tidal Range (m)-Bordeaux			
	Mean	Median	SD	Mean	Median	SD	Mean	Median	SD	N
Total	579	334	556	4.1	4.1	0.8	4.7	4.7	0.7	41
Sp	778	654	358	4.7	5.2	1.2	5.2	5.4	0.9	6
Su	267	218	110	4.0	4.3	0.7	4.7	4.8	0.6	13
Au	399	253	336	3.6	3.6	0.5	4.6	4.5	0.5	15
Wi	1,260	1,149	777	4.6	4.6	0.8	4.8	5.1	0.9	7

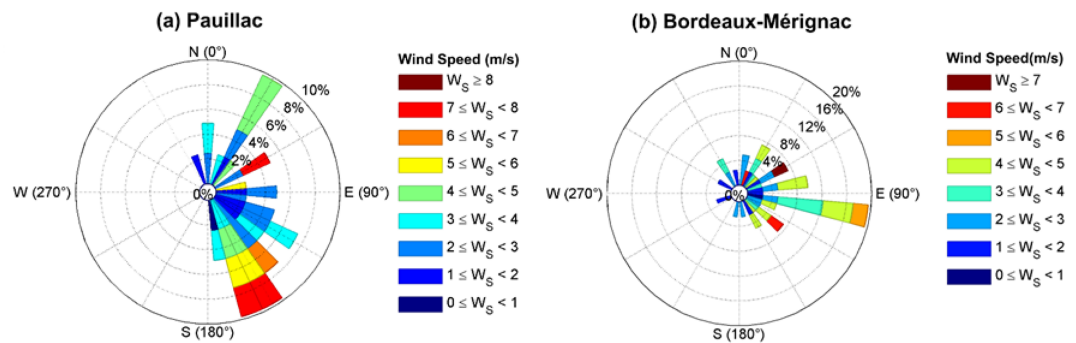*Note.* Sp: spring; Su: summer; Au: Autumn; Wi: winter.

Figure 3. Distribution of wind speed (m/s) and direction at (a) Pauillac and (b) Bordeaux-Mérignac.

the seasonal distribution heterogeneity. The mean daily river discharge value associated with the dataset is 579 ± 556 m^3/s, while the mean value over the whole period is 773 ± 676 m^3/s. Figure 2b indicates the high proportion of low freshwater inflow, mostly recorded during summer and fall, leading to a median value of 334 m^3/s. The lowest mean seasonal value (267 ± 110 m^3/s) is found in summer, while the highest value ($1,260 \pm 777$ m^3/s) is reached in winter (Table 4). Tidal range is less impacted by the seasonal distribution heterogeneity as its cycle is fortnightly. Observations in Pauillac and Bordeaux are normally distributed (Figure 2c) and the mean values (4.1 ± 0.8 m and 4.7 ± 0.7 m, respectively) are similar from the means computed between January 2005 and July 2014 by Jalón-Rojas et al. (2015). However, it is interesting to note that tidal range shows lower mean values in summer and fall similarly to daily river discharges. Correlation between these two variables ($r = 0.34$) is significant at the significant level of 5%. Finally, the distribution of images per tidal stage shows more ebb and flood situations than high and low tides (Figure 2d). This distribution is statistically in agreement with the duration of these different tidal stages. For example, the mean duration of ebb, flood, high tide and low tide at Pauillac are 7 hr, 4 hr 40, 30 min, and 15 min, respectively. The distributions of wind speed and direction in Pauillac and Bordeaux-Mérignac are presented in Figure 3. The mean values of wind speed are 4 and 3 m/s, respectively, while the wind direction is mainly oriented toward South East in Pauillac and East in Bordeaux-Mérignac.

4.2. Intercomparison Exercise Between Three SPM Models

A qualitative assessment of the performances of SPM inverse algorithms is required in order to select the most relevant approach for the Gironde FES. Descriptive statistics of the SPM distribution associated with four different subareas of the Gironde FES are estimated (Figure 4). For each subarea, statistics are separately provided for SPM derived using Nechad10, Han16, and Novoa17 algorithms, using the 41 HR multispectral images. From our dataset, a similar general statistical behavior for the three different inverse algorithms is observed. Regardless of the model, SPM values increase on average toward upstream. Except for the lower estuary characterized by medium turbid waters, Nechad10 shows a higher proportion of low SPM values than Han16 and Novoa17. For instance, the median value increases from 81 (downstream) to 259 g/m^3 (Garonne River) for Nechad10, from 118 to 318 g/m^3 for Han16, and from 76 to 412 g/m^3 for Novoa17. Furthermore, in the four subareas, Nechad10 presents a large number of extreme values higher than 1.5 times the inter-quartile distance. A total of 0.3% of the whole observations exhibit values higher than 10,000 g/m^3. These results highlight the inherent limitation of Nechad10 due to the calibration data (Han et al., 2016). Additionally, Figure 4 shows that Novoa17 provides SPM values over a higher range than Han16. For instance, the inter-quartile distances for Novoa17 are 226, 461, 537, and 607 g/m^3, in the downstream, upstream, Garonne, and Dordogne River, respectively, while the inter-quartile distances for Han16 are 205, 152, 142, and 174 g/m^3. Descriptive statistics associated with Novoa17-retrieved SPM distributions are clearly more consistent with previous results (Doxaran et al., 2009) than with Nechad10- and Han16-retrieved SPM distributions.

Average SPM values estimated by the three methods are inter-compared through direct correlation and analysis of their mean relative differences. The corresponding maps are presented in Figure 5. The scatterplots between Nechad10-Han16 (Figure 5a) and Nechad10-Novoa17 (Figure 5b) exhibit a significantly lower correlation than the scatterplot between Novoa17 and Han16 (Figure 5c). The values of the coefficient of
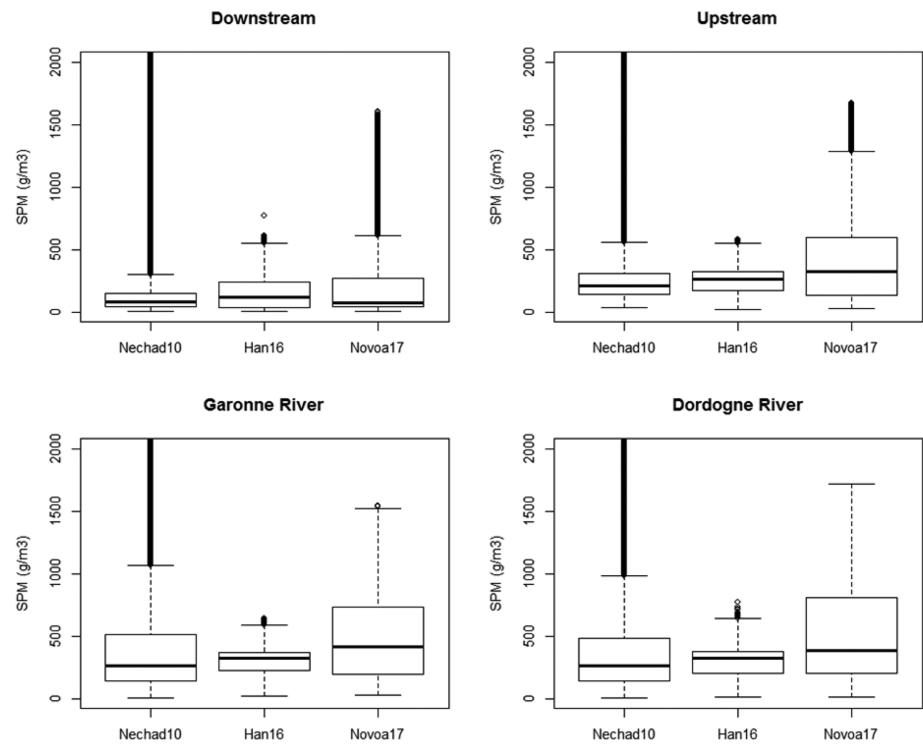
Figure 4. Boxplots of suspended particulate matter (SPM) concentration in the four subareas (lower estuary, upper estuary, Garonne River, and Dordogne River) of the Gironde FES. SPM were calculated from the algorithms of Nechad et al. (2010) (Nechad10), Han et al. (2016) (Han16), and Novoa et al. (2017) (Novoa17), applied to 20 Landsat-8/OLI and 21 Sentinel-2/MSI images acquired between years January 2013 and August 2018. Within the boxes, bold lines represent median, and lower and upper hinges represent first and third quartiles. At maximum, bars correspond to 1.5 times the interquartile distance and solid circles correspond to observations outside the bars.

determination (R^2) are 0.59, 0.45, and 0.81, respectively. A part of the noise in the relationships with Nechad10 can be directly attributed to the over-estimation of SPM at high concentration range (>100 g/m^3). Figures 5a and 5b show, for Nechad10, a large number of average SPM values higher than 1,000 g/m^3 compared to Han16 and Novoa17. Additionally, Novoa17 shows higher SPM retrievals than Han16, with a slope value of 1.89 for the regression line (Figure 5c).

Spatial distribution of the mean relative difference between Nechad10 and Han16, Nechad10 and Novoa17, and Novoa17 and Han16 are presented on Figures 5d, 5e, and 5f. It is worth noticing that the highest differences observed between Nechad10-Han16 and Nechad10-Novoa17 are located in the central (close to Pauillac) and in the tidal river parts of the Gironde FES (Figures 5d and 5e). These areas are the locations of the ETM during the periods of high and low river flow, respectively (Doxaran et al., 2009). Spatial distribution of the mean relative difference between Novoa17 and Han16 shows a longitudinal gradient with low and high differences in the downstream and upstream part of the estuary, respectively (Figure 5f). This is consistent with previous results (Han et al., 2016). They highlight the limitation of Han16 when using R_{rs} in the red bands, as input in SAA for high turbid waters (SAA-HR), and the need to use R_{rs} in the near-infrared bands (SAA-HNIR). As reported in Novoa et al. (2017), R_{rs} in the red bands is less sensitive to SPM variations than R_{rs} in the NIR bands when concentrations are higher than 50 g/m^3.

The successive analysis of the descriptive statistics of the SPM products generated by the three different algorithms and results of the inter-comparison exercise clearly indicate that Novoa17, which was specifically developed on Gironde Estuary data set, is the most relevant algorithm to reproduce the three-order-of-magnitude range of SPM (Jalón-Rojas et al., 2015). In the next sections, SPM will be then retrieved from Novoa17. For brevity, we suppress the reference to Novoa17 in the following text.
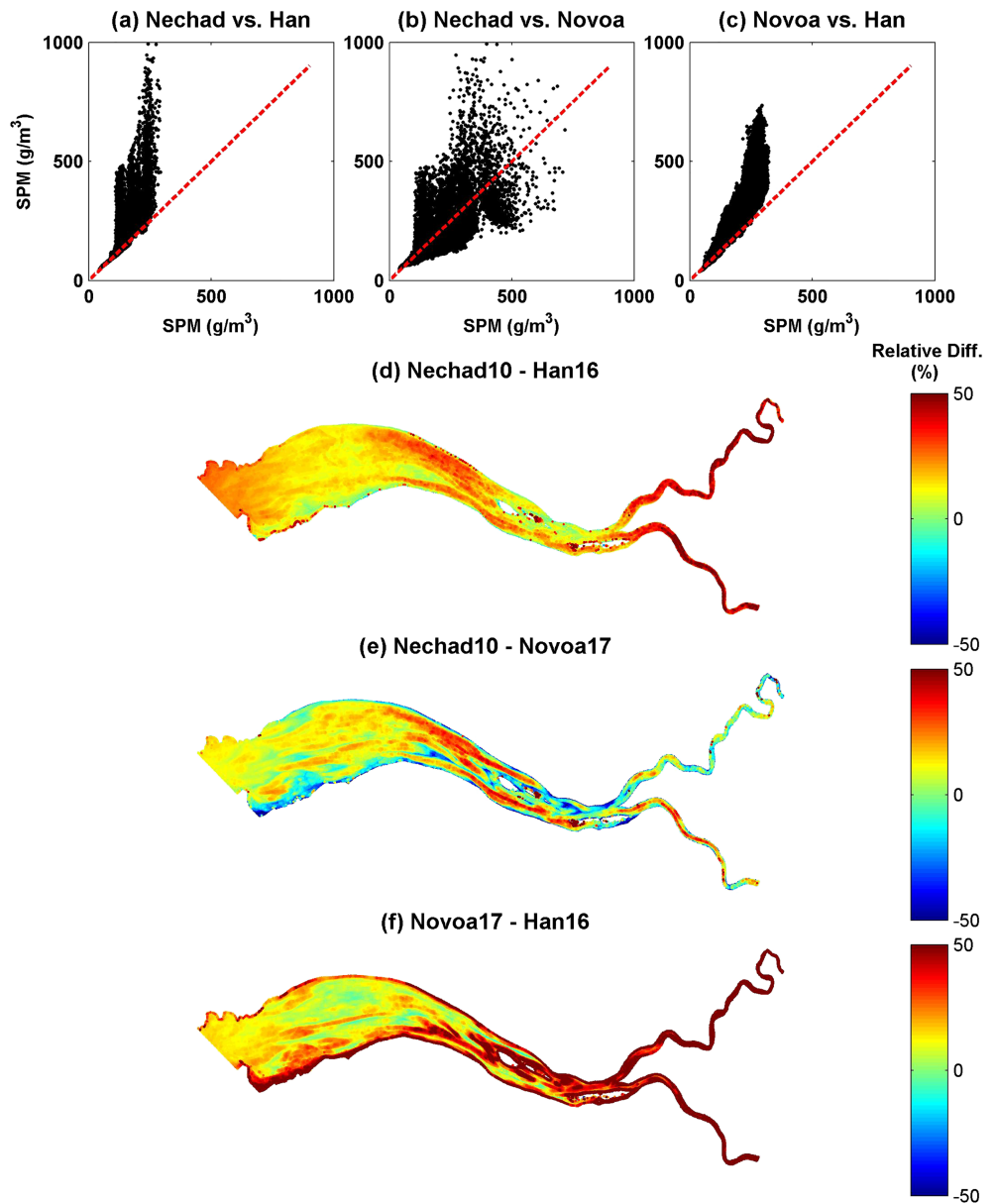
Figure 5. Comparisons of average (computed for each pixel of the Gironde Estuary from the 20 Landsat-8/OLI and 21 Sentinel-2/MSI images acquired over 2013-2018) suspended particulate matter (SPM) values (g/m^3) estimated using the three different inversion algorithms and spatial distribution of their mean relative difference (given in %). Comparison is successively performed on the pair (a–d) Nechad10 and Han16, (b–e) Nechad10 and Novoa17, (c–f) and Novoa17 and Han16. Red dashed lines represent 1:1 line.

4.3. SPM Averaged Spatial Distribution

The spatial distribution of the pixel-averaged SPM values was computed from the whole Landsat-8/OLI and Sentinel-2/MSI images dataset ($N = 41$) and for different environmental conditions, combining high/low tidal range in Pauillac and high/low daily river discharges. The median value (Table 2) is used as criteria to separate high and low values. The averaged-SPM spatial distribution (Figure 6a) exhibits a typical along-estuary gradient. SPM values increase in the upstream direction, ranging from 100 g/m^3 at Le Verdon, 350 g/m^3 in Pauillac to 450 g/m^3 and 500 g/m^3 in Bordeaux and Libourne, respectively. Although this general pattern strongly depends on the representativeness of the environmental conditions associated with the dataset, it is characteristic of the SPM average annual distribution in the Gironde FES.
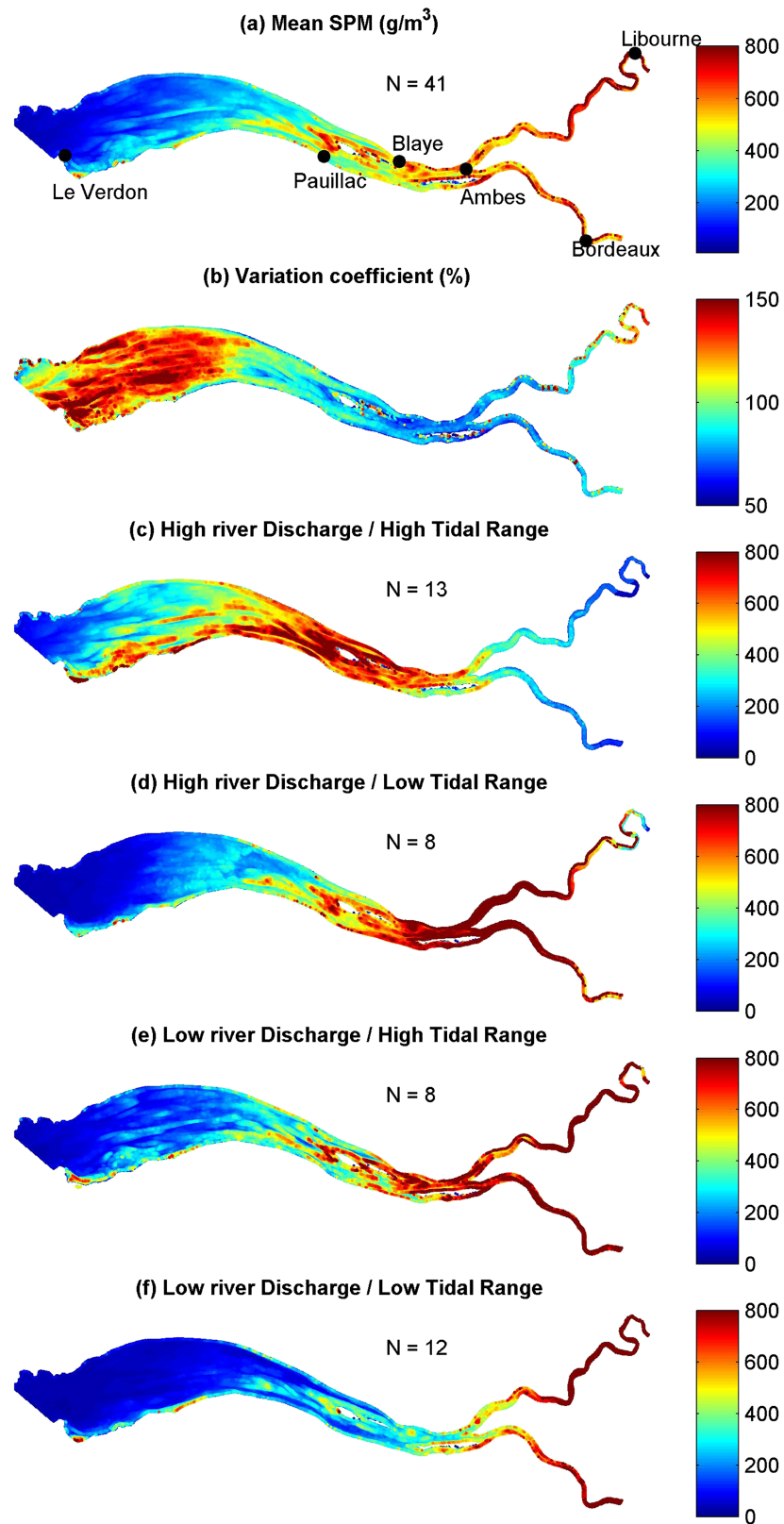
Figure 6. (a) Spatial distribution of averaged suspended particulate matter (SPM) concentration (g/m^3) estimated using 41 Landsat-8/OLI and Sentinel-2/MSI images available over the July 2013 to August 2018 period, (b) the associated variation coefficient (%), and (c) averaged SPM values associated with high daily river discharges/high tidal range ($N = 13$), (d) high daily river discharges/low tidal range ($N = 8$), (e) low daily river discharges/high tidal range ($N = 8$), and (f) low daily river discharges/low tidal range ($N = 12$) in the whole Gironde FES.

Two local areas associated with high SPM values can be observed in the mid-reaches (close to Pauillac and Blaye). These areas exhibit a low value of the variation coefficient (Figure 6b), which indicate the presence of static or main ETM (Doxaran et al., 2009; Maanen & Sottolichio, 2018). Figure 1b clearly shows that these two local areas are associated with singular bathymetric features, including strong lateral gradients, low bathymetry values, and the presence of islands. The highest values of the coefficient of variation (Figure 6b) are located over a large area in the lower reaches. More specifically, local zones associated with shallow waters present values higher than 150%. These zones correspond to secondary or dynamic ETM (Doxaran et al., 2009).

At the seasonal timescale, spring-neap cycles and river inflow variations are the main factors ruling the spatial distribution of SPM (Jalón-Rojas et al., 2017). High river inflow causes the downstream migration of the ETM and thus the increase of SPM in the lower reaches and midreaches (upper) and the decrease in the tidal rivers (Figures 6c and 6d), compared with the low river flow situation (Figures 6e and 6f). Moreover, the spring-neap tidal cycle clearly shows a significant impact on the turbidity signal magnitude. Spring tide conditions, which generate higher currents velocities than neap tides, are associated with the highest SPM values (Figures 6c and 6e). It is interesting to note here that the secondary ETM occurs during spring tides regardless of river inflow conditions.

4.4. Main SPM T-Mode Patterns

The T-mode PCA results highlight three dominant spatial patterns of the SPM distribution. The three first principal components together account for 65.7% of the total variance in the dataset. Individually, they explain 43.5%, 15.0%, and 7.2 % of the variance. The spatial (components) and temporal (loadings) patterns associated with three SPM modes are shown in Figure 7. The first principal component (PC1) displays the same SPM distribution over the entire domain than the mean signal (Figure 7a). High loading values can be observed from each satellite image date (Figure 8a), with a mean value of 0.64 ± 0.17. Only images number 5 (7 March 2014) and 25 (10 March 2017) exhibit a low correlation value ($r < 0.30$). It is worth to note that these two images were acquired during intense winter flood events with a discharge peak of 2,632 and 2,075 m^3/s, respectively. Further, PC1 loading is strongly negatively correlated with tidal range and daily river discharge (-0.62 and -0.73, respectively, Table 5). This result highlights that PC1 is mainly representative of a SPM spatial distribution associated with low tidal range and low daily river discharge conditions. The second principal component (PC2) exhibits an out-of-phase relationship between SPM anomalies located in the mid-reaches and in the lower and upper areas (Figure 7b). Loadings accentuate differences between high tidal range—high freshwater inflow (positive correlation) and low tidal range—low freshwater inflow (negative correlation) conditions (Figure 8b). Correlations between PC2 loading and environmental forcing are statistically significant for the tidal range, freshwater inflow, and water depth with a value of 0.68, 0.65, and -0.33, respectively (Table 5). The third principal component (PC3) displays a negative correlation between SPM anomalies in shallow waters located on sand banks and mudflats, and deeper waters in the main channel. PC3 loadings exhibit low-to-moderate values, excepted for images number 17 (22 August 2016), 18 (21 September 2016), 19 (6 October 2016), 32 (26 October 2017), and 33 (31 October 2017), for which water depth and wind speed show values significantly higher and lower than the mean, respectively. Correlations of the loadings with the water depth ($r = 0.58$) and wind speed ($r = -0.32$) are consistent with this result.

Temporal patterns associated with the loadings of the three first principal components, and more specifically for PC1 and PC2, exhibit a very clear seasonal cycle between 2013 and July 2016. From July 2016, time series reveals shorter oscillations. These temporal patterns highlight the statistical bias generated by the limited number of observations. The higher is the number of observation, the higher is the capability to record high frequency variations due to environmental forcing, such as fortnightly and semidiurnal tide cycles. The HRS multispectral image archive provides four periods for which three or more satellite images were acquired successively in a time interval of less than one month. For instance, four images have been recorded in October 2016 (6, 10, 22, and 31; see Figure 8). For this period, the values of the daily river discharge (157–241 m^3/s) are significantly lower than the mean value computed for the whole period (Table 4), while the tidal range (3.6–4.3 m in Pauillac) exhibits more contrasted conditions. Associated with these environmental conditions, PC1 Loading show a moderate variability with values comprised between 0.53 and 0.67 that indicate an explained variance ranging from 28% to 45%. On the opposite, PC2 loadings are
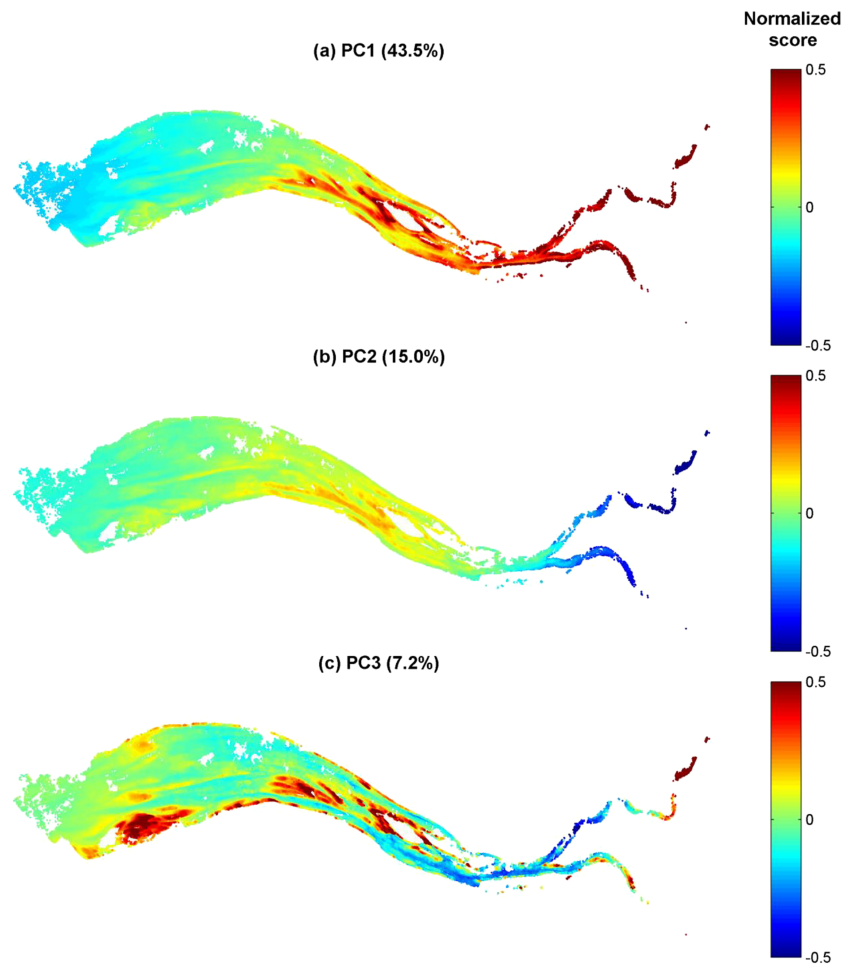
Figure 7. (a) First, (b) second, and (c) third principal components explaining 43.5%, 15.0%, and 7.2% of the total variance, respectively. Component scores are normalized and vary between −1 and +1.

characterized by a significant variability. The correlation is statistically significant only for 11 October 2016 with a value of 0.61 and an explained variance of 37%. The analysis of environmental data for this day indicates the lowest tidal range compared to the three other dates. Moreover, the water depth value (4.4 m) in Pauillac, associated with high tide conditions, is the highest over the whole dataset. In April 2017, three successive acquisitions (9,29, see Figure 8) are available. For this period, the mean value of the daily river discharge (523 m^3/s) is close to the mean value of the dataset. However, the tidal range (5.3, 2.5, and 4.9 m in Pauillac) exhibits sharp variations due to the spring-neap tide cycle. PC1 and PC2 loadings show a significant variability with values comprised between 0.54–0.88 and −0.15–0.57, that is, 29–77% and 2–32% of the explained variance, respectively. In October 2016 and April 2017, the spatial distribution of SPM statistically well described by the two first principal components shows a high intramonth variability (results not shown) mainly control by the fortnightly and semidiurnal tide cycles.

The total variance explained by the three first principal components for each of the images is given on Figure 8d. Only eight images present a total explained variance lower than 50%, which indicates a low representativity of the three first principal components for describing the spatial distribution of SPM. The total explained variance is particularly low for the three images acquired on 10 July 2013, 7 March 2014, and 15 March 2017. On 10 July 2013, the values of the tidal range (4.5 in Pauillac) and the daily river discharge (515 m^3/s) are close to the average hydrodynamics state. But, the image was acquired with moderately strong south west wind conditions (5 m/s) and during the low tide in Le Verdon, associated with one of the lowest water depth values (1.5 m) recorded in our dataset. These environmental conditions generate an unusual
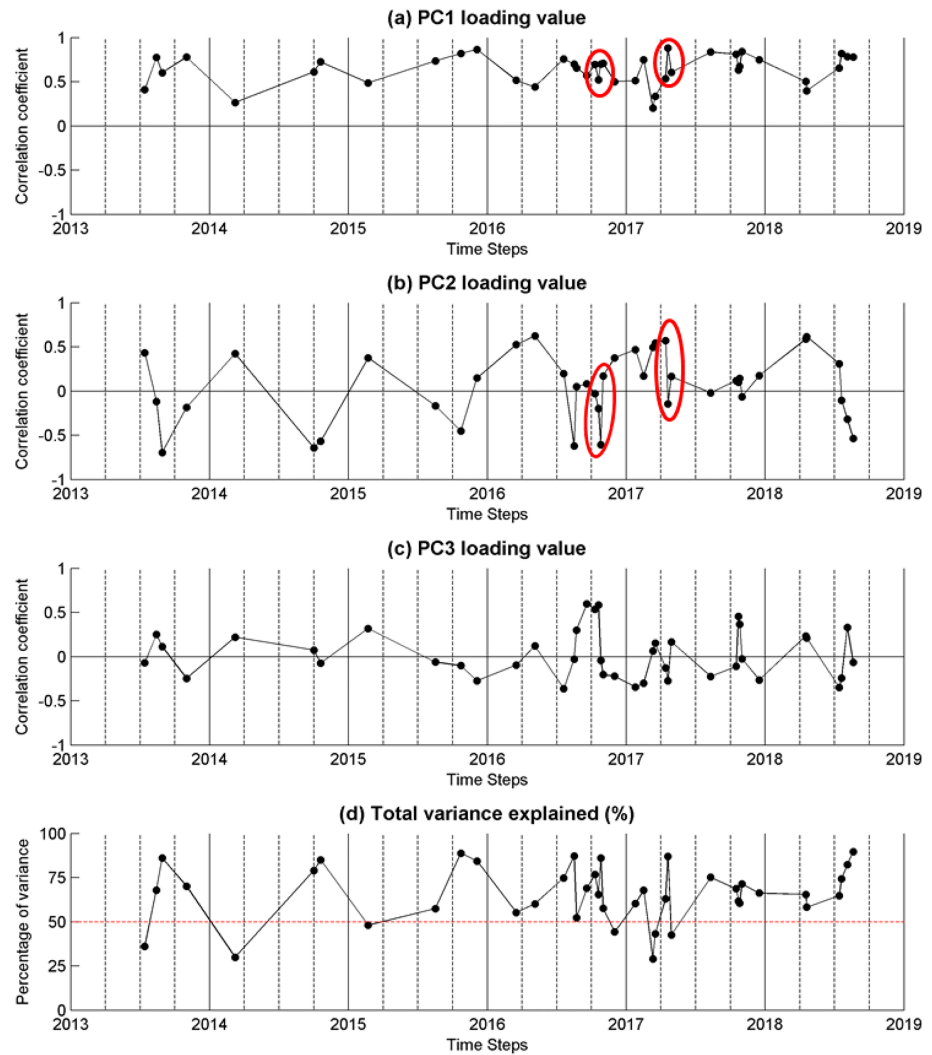
Figure 8. Loading of the (a) first, (b) second, (c) third principal components and (d) total variance explained for each image. The red contours are associated with two series of four and three successively acquired images in October 2016 and April 2017, respectively.

SPM distribution characterized by along-estuary rectilinear patterns of near-surface currents (Figure 9a). The 7 March 2014 and 15 March 2017 satellite images were acquired during strong flood events, with daily river discharge values of 2,632 and 2,075 m^3/s. Hydrological conditions were associated with the ebb and the low tide in Pauillac, respectively. Both images exhibit eddy-like structures in the mid-reaches between the right edge and the main channel. However, eddy-like structures are more pronounced on 15 March 2017 (Figure 9b).

4.5. Along- and Cross-Main Stream Sections

Two longitudinal transects were selected along the FES in order to describe the variability of the averaged SPM values computed from the whole Landsat-8/OLI and Sentinel-2/MSI image dataset (Figure 10). Longitudinal transects are located in the main channel and on the central shoal of the estuary (see Figures 1b and 1c), and in the middle and right side of the channel for the Garonne River (see Figure 1d). Results for the Dordogne River are not presented as they are similar to those of the Garonne River.
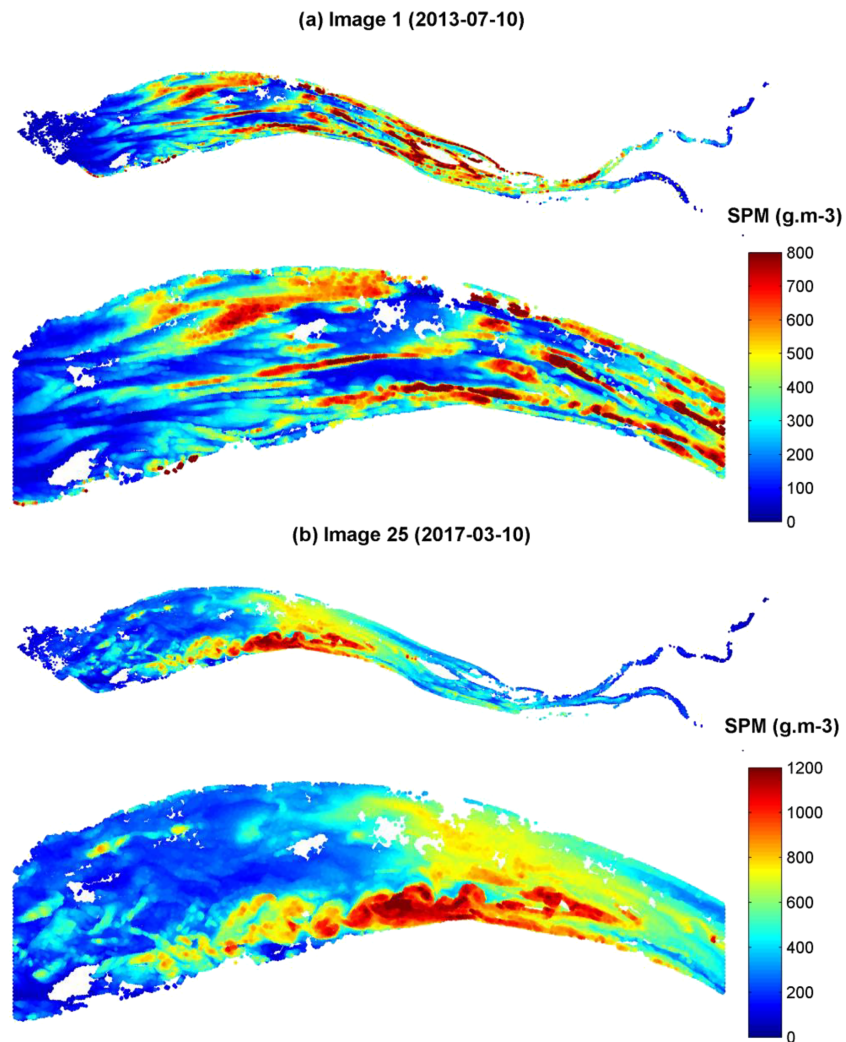
Table 5
Correlation Between Loadings of the First, Second, and Third Principal Components, and Environmental Parameters

Correlation coefficient	Tidal range	Daily river discharge	Water depth	Wind speed
PC1	−0.62*	−0.73*	−0.01	−0.09
PC2	0.68*	0.65*	−0.33*	−0.17
PC3	0.29	0.04	0.58*	−0.32*

*Significant correlations at the level of significance of 5%.

Figure 9. Mapping of the spatial distribution of suspended particulate matter (SPM; g/m³) associated with near-surface current patterns statistically under-represented in the Landsat-8/OLI and Sentinel-2/MSI images archive (N=41) for the satellite scenes acquired on (a) 10 July 2013 and (b) 10 March 2017.

As a general common pattern for the two longitudinal transects, the smoothed SPM signal shows similar large-scale increasing concentrations from the mouth (km 0) to Bordeaux (km 95) (Figures 8a and 8c). SPM values increase approximately from 20 to 550 g/m³ in average. These average values correspond to the typical along-estuary gradient described in the previous section (Figure 6), which is characteristic of the SPM average annual distribution in the Gironde FES.

However, significant differences in concentration must be noted at the subdomain scale. The increase in concentration above the main channel is uniform from Le Verdon to Bec d'Ambès, with very low fluctuations (Figure 10a). But relative increase of concentration is observed between km 20 to 45, and more abrupt increase is observed in the Garonne River at km 80 and 90. A comparison with the bathymetric profile suggests that increase in concentration occur in areas where depth decreases. Concentration along the shoals confirms this pattern, but shows higher local variability (Figure 10c). In addition to the low increase found between km 30 and 40, a series of concentration peaks are observed between km 45 and 100. The majority of them correspond to shallow areas, as proven by the bathymetric profile plotted in the same figure. The only exception to this trend is the main concentration peak found in Pauillac (700 g/m³), which does not correspond to a shoal but to a pit in an area surrounded by shoals and mudbanks.
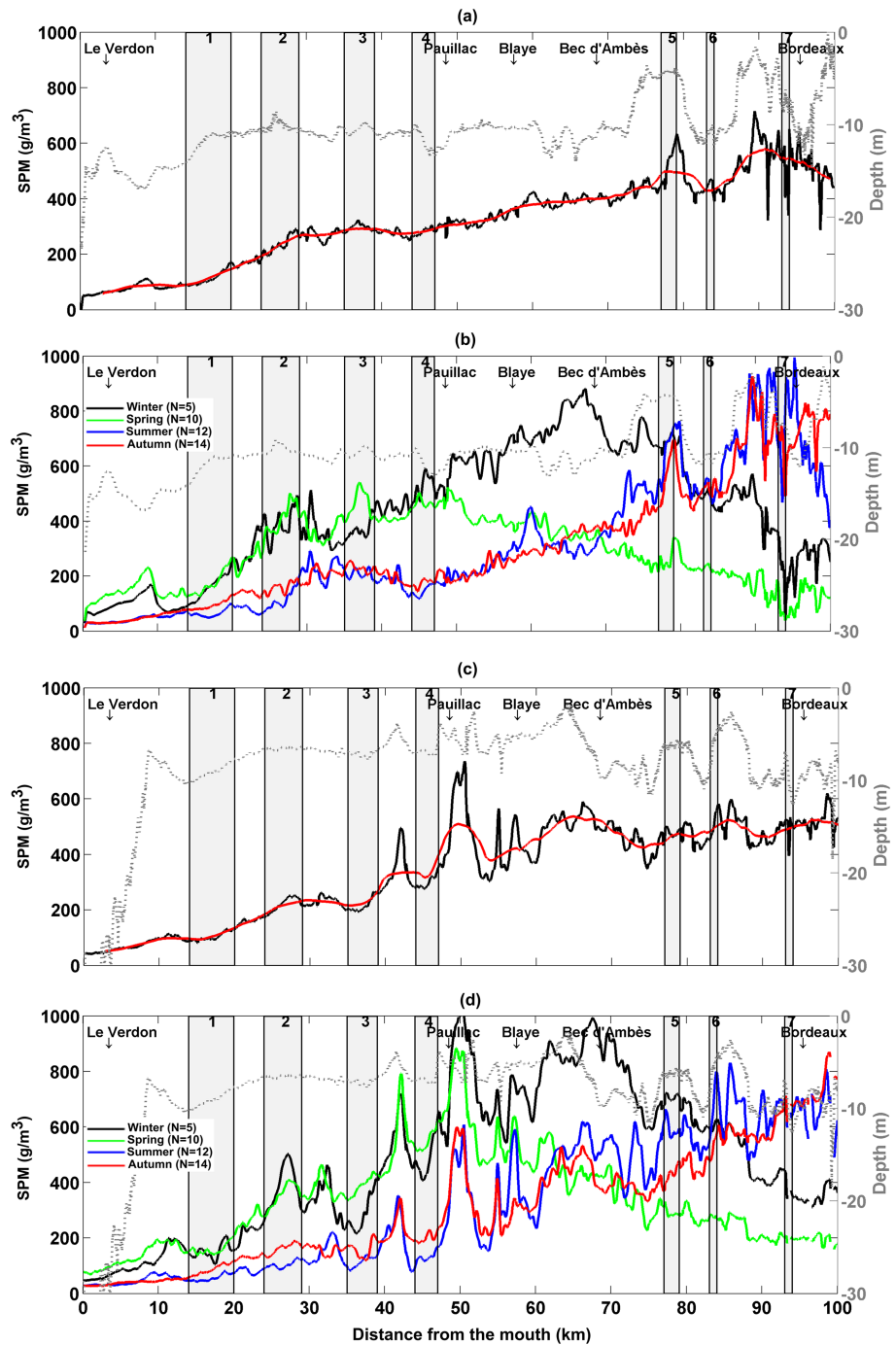
Figure 10. Longitudinal distribution of averaged suspended particulate matter (SPM) values (g/m^3) computed from all the Landsat-8/OLI and Sentinel-2/MSI images ($N = 41$) over the February 2013 to August 2018 period in the Gironde FES from the mouth to Bordeaux (a) on the main channel and (c) in the central shoal. The red line is the smoothing SPM signal. Seasonal longitudinal distributions are represented (b) on the main channel and (d) in the central shoal. The dashed grey line is the depth, and the seven grey boxes are the zones associated with transverse transects (see Figures 1b and 1d for their location). Main cities along the Gironde FES are indicated in black with arrows (see Figures 1b–1d for their locations).

Longitudinal distributions of averaged SPM were determined for the four seasons on the main channel (Figure 10b). During winter and spring seasons, the maximum concentration of SPM is found in the middle reaches of the estuary. In spring, highest values (450 g/m^3) are found between km 37 and 50,
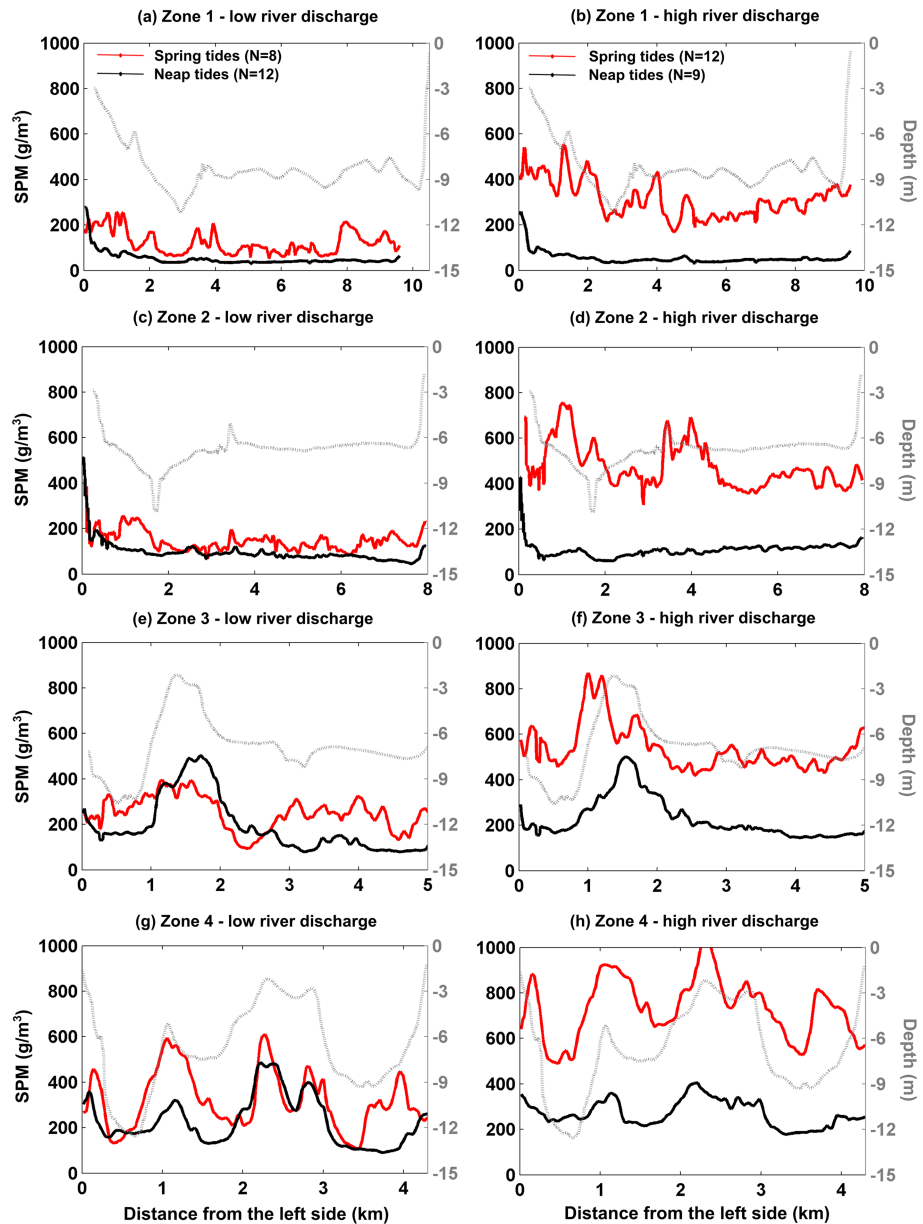
Figure 11. Transverse variability of averaged suspended particulate matter (SPM) value (g/m^3) over the February 2013-August 2018 period classified in (a, c, e, and g) low rivers discharges and (b, d, f, and h) high river discharges. The four shaded boxes in Figure 1 are represented here: (a) and (b) for the box 1, (c) and (d) for the box 2, (e) and (f) for the box 3, and (g) and (h) for the box 4. The red line is corresponding to averaged SPM during spring tides and black line during neap tides. The bathymetry is represented in grey line.

while in winter, highest values (750 g/m^3) are found more upstream, close to the confluence (km 68). This seasonal distribution of SPM is closely correlated to river discharges (Table 2) in accordance with previous publications (Jalón-Rojas et al., 2015). However, a remarkable pattern not documented before is the very similar SPM profile between the mouth and km 50. During summer and autumn, the SPM distributions are also remarkably similar all along the longitudinal axis. The maximum concentration is found in the fluvial part, with SPM values reaching approximately 800 g/m^3. Downstream, SPM decreases progressively to less than 20 g/m^3. Distribution in the central shoals (Figure 10d) shows similar trends than those for the channel, but with higher variability, as described previously.

The above mentioned features suggests a strong bathymetric control on SPM gradients. This is confirmed by the analysis of cross-estuary profiles. Among the 7 zones presented as grey boxes in Figures 1 and 10, four zones located in the lower estuary were selected to compare averaged SPM and bathymetry (Figure 11). For each box, average SPM signal is shown for different tidal and fluvial conditions. The median value of river discharges is 321 m³/s, thus high river and low rover discharges are considered relative to this value. Average SPM during low river discharges are presented in Figures 11a, 11c, 11e, and 11g (left column), high river discharges in Figures 11b, 11d, 11f, and 11h. Therefore, for each case, average SPM signal is split into neap and spring tides conditions.

During low river discharge, when the turbidity maximum shifts toward the upper estuary, SPM values in the lower estuary are weak and SPM are slightly higher during spring tides compared to neaps (left panel of Figure 11). In zones 1 and 2, SPM shows also higher spatial variability during spring than neap tides (Figures 11a and 11c), which is coherent with more turbulent conditions during spring tides. In zones 3 and 4, a larger scale spatial variability is observed, which may be linked to the bathymetric gradients shown by the depth profile (Figures 11e and 11g). In general, as already shown in Figure 10, SPM is higher on the shoals and lower in the channels, and the pattern is similar during spring and neap tides.

During high river flow conditions, the turbidity maximum shifts to the central and lower estuary and therefore averaged SPM are much higher (right panels in Figure 11). Also, differences between spring and neap tides conditions are larger; thus patterns observed for the low discharge conditions are exacerbated here. In zones 1 and 2 (Figures 11b and 11d), SPM during spring tides are higher and show strong spatial variability. In zones 3 and 4 (Figures 11f and 11h) the alternance of channels and shoals clearly controls the lateral SPM gradients.

This features described here through high-resolution surface SPM give new insights of the distribution of SPM in the Gironde estuary. In particular, the strong control of local bathymetry leads to remarkably persistent patterns of SPM gradients despite changes in hydrological conditions. This is consistent with previous findings in the Hudson River (Ralston et al., 2012). The analysis of physical processes explaining these trends are beyond the scope of this paper and need to be further investigated. However, it can advance that better mixing in shallow areas, combined to more dilution in the water column above deeper areas result in higher surface SPM on shoals and lower SPM on the deeper areas. The role of wind-waves can also be significant in very shallow areas, but it is assumed that this effect may be limited to the lower estuary at high tide, where estuarine sections and intertidal areas are wide, allowing longer fetch and stronger resuspension flux.

5. Conclusion

In this study, we analyzed statistically the spatial variability of surface SPM in the Gironde FES using a high resolution satellite multispectral data archive composed of Landsat-8/OLI and Sentinel-2/MSI images. First, a T-mode orientation spectral decomposition allowed to quantify the contribution of the main spatial patterns of SPM to the total variance and the contribution of each environmental forcing. As expected, the tidal range and the daily river discharge are the main forcing, which control the longitudinal gradient of the SPM distribution. However, we demonstrated also the significant impact of the water depth, which depends on the tidal cycles, and the wind speed on the lateral distribution of SPM. In particular, in the lower area of the estuary, strong lateral gradients located between the shoals and deeper areas are positively correlated with the water depth and negatively correlated with the wind speed. This strong lateral heterogeneity of SPM could be directly associated with a lower lateral sediment transport during high tide and low wind conditions. Then, a descriptive analysis of the SPM variability along longitudinal and transverse-estuary sections was conducted. Results highlight the strong control of local bathymetry on the surface SPM distribution. In particular, we identified clearly that the maxima of surface turbidity are not located in the main channel but on the shoals.

Due to a low temporal resolution, high spatial resolution multispectral missions provide discontinuous time series. As a consequence, the total number of images is considerably reduced compared to medium resolution missions. This reduce number of data can generate some analytical biases. For example, in our dataset composed of 41 images, the tidal range is significantly correlated to the water discharge. This may generate an over-representation of a given type of environmental conditions and of the associated SPM distribution. However, this study demonstrates the high potential of T-mode spectral decomposition to analyze

discontinuous time series. Further, the main spatial patterns could be used in future researches for spatio-temporal multi-sensor fusion (Belgiu & Stein, 2019; Wu et al., 2013). Further analysis of physical processes with process-based modeling may help to explain and understand patterns observed by remote sensing. However, a spatial resolution similar to that achieved by the images is necessary to make the analysis relevant to the findings of the present study.

References

Allen, G. P., Bonnefille, R., Courtois, G., & Migniot, C. (1974). Processus de sédimentation des vases dans l'estuaire de la Gironde. *La Houille Blanche*, 1-2, 129–136. https://doi.org/10.1051/lhb/1974013

Allen, G. P., Salomon, J. C., Bassoullet, P., Dupenhoat, Y., & Degrandpre, C. (1980). Effects of Tides on Mixing and Suspended Sediment Transport in Macro-Tidal Estuaries. *Sedimentary Geology*, 26(1-3), 69–90. https://doi.org/10.1016/0037-0738(80)90006-8

Barsi, J. A., Lee, K., Kvaran, G., Markham, B. L., & Pedelty, J. A. (2014). The spectral response of the Landsat-8 Operational Land Imager. *Remote Sensing*, 6, 10,232–10,251. https://doi.org/10.3390/rs61010232

Belgiu, M., & Stein, A. (2019). Spatiotemporal image fusion in remote sensing. *Remote Sensing*, 11, 818. https://doi.org/10.3390/rs11070818

Bierman, P., Lewis, M., Ostendorf, B., & Tanner, J. (2011). A review of methods for analysing spatial and temporal patterns in coastal water quality. *Ecological Indicators*, 11, 103–114. https://doi.org/10.1016/j.ecolind.2009.11.001

Blondeau-Patissier, D., Gower, J., Dekker, A. G., Phinn, S. R., & Brando, V. E. (2014). A review of ocean color remote sensing methods and statistical techniques for the detection, mapping and analysis of phytoplankton blooms in coastal and open oceans. *Progress in Oceanography*, 123, 123–144. https://doi.org/10.1016/j.pocean.2013.12.008

Bonneton, P., Bonneton, N., Parisot, J.-P., & Castelle, B. (2015). Tidal bore dynamics in funnel-shaped estuaries. *Journal of Geophysical Research: Oceans*, 120, 923–941. https://doi.org/10.1002/2014JC010267

Bru, D., Lubac, B., Normandin, C., Robinet, A., Leconte, M., Hagolle, O., et al. (2017). Atmospheric correction of multi-spectral littoral images using a PHOTONS/AERONET-based regional aerosol model. *Remote Sensing*, 9(8), 814. https://doi.org/10.3390/rs9080814

Caballero, I., Steinmetz, F., & Navarro, G. (2018). Evaluation of the first year of operational Sentinel-2A data for retrieval of suspended solids in medium- to high-turbidity waters. *Remote Sensing*, 10(7). https://doi.org/10.3390/rs10070982

Castaing, P., Jouanneau, J. M., Prieur, D., Rangel-Davalos, C., & Romana, L. A. (1984). Variations spatio-temporelles de la granulométrie des suspensions de l'estuaire de la Gironde. *J. Rech. Océanogr*, 9, 115–119.

Coynel A. (2005). Érosion mécanique des sols et transferts géochimiques dans le bassin Adour-Garonne. Doctorat de l'Université Bordeaux 1, 572 p.

Coynel A., Blanc G., Dutruch L., Bossy C., Lerat A., Gil-Diaz T., et al. (2018). Évolution des flux de MES (1994-2016) et de cadmium (1999-2016) dans le système Riou-Mort-Lot-Garonne, Rapport contrat AEAG, 24 p.

Dogliotti, A. I., Ruddick, K., & Guerrero, R. (2016). Seasonal and inter-annual turbidity variability in the Rio de la Plata from 15 years of MODIS (2016): El Nino dilution effect. *Estuarine, Coastal and Shelf Science*, 182, 27–39. https://doi.org/10.1016/j.ecss.2016.09.013

Doxaran, D., Froidefond, J. M., Castaing, P., & Babin, M. (2009). Dynamics of the turbidity maximum zone in a macrotidal estuary (the Gironde, France): Observations from field and MODIS satellite data. *Estuarine, Coastal and Shelf Science*, 81, 321–332. https://doi.org/10.1016/j.ecss.2008.11.013

Druine, F., Verney, R., Deloffre, J., Lemoine, J.-P., Chapalain, M., Landemaine, V., & Lafite, R. (2018). In situ high frequency long term measurements of suspended sediment concentration in turbid estuarine system (Seine Estuary, France) : Optical turbidity sensors response to suspended sediment characteristics. *Marine Geology*, 400, 24–37. https://doi.org/10.1016/j.margeo.2018.03.003

Drusch, M., del Bello, U., Carlier, S., Colin, O., Fernandez, V., Gascon, F., et al. (2012). Sentinel-2: ESA's Optical High-Resolution Mission for GMES Operational Services. *Remote Sensing of Environment*, 120, 25–36. https://doi.org/10.1016/j.rse.2011.11.026

Dyer, K. R. (1988). Fine sediment particle transport in estuaries. In J. Dronkers & W. van Leussen (Eds.), *Physical Process in Estuaries* (pp. 427–445). Berlin Heidelberg: Springer. https://doi.org/10.1007/978-3-642-73691-9_16

Etcheber, H., Taillez, A., Abril, G., Garnier, J., Servais, P., Moatar, F., & Commarieu, M. V. (2007). Particulate organic carbon in the estuarine turbidity maxima of the Gironde, Loire and Seine estuaries: origin and lability. *Hydrobiologia*, 588, 245–259. https://doi.org/10.1007/s10750-007-0667-9

Feng, L., Hu, C., Chen, X., & Song, Q. (2014). Influence of the Three Gorges Dam on total suspended matters in the Yangtze Estuary and its adjacent coastal waters: Observations from MODIS. *Remote Sensing of Environment*, 140, 779–788. https://doi.org/10.1016/j.rse.2013.10.002

French, J. R., Burningham, H., & Benson, T. (2008). Tidal and Meteorological Forcing of Suspended Sediment Flux in a Muddy Mesotidal Estuary. *Estuaries and Coasts*, 31(5), 843–859. https://doi.org/10.1007/s12237-008-9072-5

Garel, E., Nunes, S., & Neto, J. M. (2009). The autonomous Simpatico system for real-time continuous water-quality and current velocity monitoring: examples of application in three Portuguese estuaries. *Geo-Marine Letters*, 29(5), 331–341. https://doi.org/10.1007/s00367-009-0147-5

Gernez, P., Lafon, V., Lerouxel, A., Curti, C., Lubac, B., Cerisier, S., & Barillé, L. (2015). Toward sentinel-2 high resolution remote sensing of suspended particulate matter in very turbid waters: SPOT4 (take5) experiment in the Loire and Gironde estuaries. *Remote Sensing*, 7, 9507–9528. https://doi.org/10.3390/rs70809507

Grasso, F., & Le Hir, P. (2019). Influence of morphological changes on suspended sediment dynamics in a macrotidal estuary: diachronic analysis in the Seine Estuary (France) from 1960 to 2010. *Ocean Dynamics*, 69(1), 83–100. https://doi.org/10.1007/s10236-018-1233-x

Han, B., Loisel, H., Vantrepotte, V., Mériaux, X., Bryère, P., Ouillon, S., et al. (2016). Development of a semi-analytical algorithm for the retrieval of suspended particulate matter from remote sensing over clear to very turbid waters. *Remote Sensing*, 8(3), 211. https://doi.org/10.3390/rs8030211

Hudson, A. S., Talke, S. A., & Jay, D. A. (2016). Using satellite observations to characterize the response of estuarine turbidity maxima to external forcing. *Estuaries and Coasts*, 40(2), 343–358. https://doi.org/10.1007/s12237-016-0164-3

IOCCG (2006). Remote Sensing of Inherent Optical Properties: Fundamentals, Tests of Algorithms, and Applications. In Z. Lee (Ed.), *Reports of the International Ocean-Colour Coordinating Group, No. 5*. Dartmouth, Canada: IOCCG.

IOCCG (2010). Atmospheric Correction for Remotely-Sensed Ocean-Colour Products. In M. Wang (Ed.), *Reports of the International Ocean-Colour Coordinating Group, No. 10*. Dartmouth, Canada: IOCCG.

Jalón-Rojas, I., Schmidt, S., & Sottolichio, A. (2015). Turbidity in the fluvial Gironde estuary (southwest France) based on 10-year continuous monitoring: sensitivity to hydrological conditions. *Hydrology and Earth System Sciences*, *19*, 2805–2819. https://doi.org/10.5194/hess-19-2805-2015

Jalón-Rojas, I., Schmidt, S., & Sottolichio, A. (2016). Evaluation of spectral methods for high-frequency multiannual time series in coastal transitional waters: Advantages of combined analyses. *Limnology and Oceanography: Methods*, *14*, 381–396. https://doi.org/10.1002/lom3.10097

Jalón-Rojas, I., Schmidt, S., & Sottolichio, A. (2017). Comparison of environmental forcings affecting suspended sediments variability in two macrotidal, highly-turbid estuaries. *Estuarine, Coastal and Shelf Science*, *198*, 529–541. https://doi.org/10.1016/j.ecss.2017.02.017

Jalón-Rojas, I., Sottolichio, A., Hanquiez, V., Fort, A., & Schmidt, S. (2018). To what extent multidecadal changes in morphology and fluvial discharge impact tide in a convergent (turbid) tidal river. *Journal of Geophysical Research: Oceans*, *123*, 3241–3258. https://doi.org/10.1002/2017JC013466

Jay, D. A., Talke, S. A., Hudson, A. S., & Twardowski, M. (2015). Estuarine turbidity maxima revisited: instrumental approaches, remote sensing, modeling studies, and new directions. In P. J. Ashworth, J. L. Best, & D. R. Parsons (Eds.), *Developments in sedimentology: fluvial-tidal sedimentology* (pp. 49–109). Amsterdam, Netherlands: Elsevier. https://doi.org/10.1016/B978-0-444-63529-7.00004-3

Jouanneau, J. M., & Latouche, C. (1981). The Gironde estuary. In H. Füchtbauer, A. P. Lisitzy, J. D. Millerman, & E. Seibold (Eds.), *Contributions to Sedimentology* (pp. 1–115). Stuttgart: E. Schweizerbat'sche Verglagsbuchhandlung.

Kapsimalis, V., L. Masse and J.P. Tastet (2004), Tidal impact on modern sedimentary facies in the Gironde Estuary, southwestern France Journal of Coastal Research, 1-11

Loisel, H., Mangin, A., Vantrepotte, V., Dessailly, D., Ngoc Dinh, D., Garnesson, P., et al. (2014). Variability of suspended particulate matter concentration in coastal waters under the Mekong's influence from ocean color (MERIS) remote sensing over the last decade. *Remote Sensing of Environment*, *150*, 218–230. https://doi.org/10.1016/j.rse.2014.05.006

Maanen, B., & Sottolichio, A. (2018). Hydro- and sediment dynamics in the Gironde estuary (France): sensitivity to seasonal variations in river inflow and sea level rise. *Continental Shelf Research*, *165*, 37–50. https://doi.org/10.1016/j.csr.2018.06.001

Machado-Machado, E. A., Neeti, N., Eastman, J. R., & Chen, H. (2011). Implications of space-time orientation for principal components analysis of Earth observation image time series. *Earth Science Informatics*, *4*(3), 117–124. https://doi.org/10.1007/s12145-011-0082-7

Mitchell, S. B., Uncles, R. J., & Akesson, L. (2012). Observations of turbidity in the Thames estuary. *Water Environment Journal*, *26*, 511–520. https://doi.org/10.1111/j.1747-6593.2012.00311.x

Nechad, B., Ruddick, K., & Park, Y. (2010). Calibration and validation of a generic multisensor algorithm for mapping of total suspended matter in turbid waters. *Remote Sensing of Environment*, *114*, 854–866. https://doi.org/10.1016/j.rse.2009.11.022

Neeti, N., & Eastman, J. R. (2014). Novel approaches in extended principal component analysis to compare spatio-temporal patterns among multiple image time series. *Remote Sensing of Environment*, *148*, 84–96. https://doi.org/10.1016/j.rse.2014.03.015

Novoa, S., Doxaran, D., Ody, A., Vanhellemont, Q., Lafon, V., Lubac, B., & Gernez, P. (2017). Atmospheric corrections and multiconditional algorithm for multi-sensor remote sensing of suspended particulate matter in low-to-high turbidity levels coastal waters. *Remote Sensing*, *9*(1). https://doi.org/10.3390/rs9010061

Pahlevan, N., Chittimalli, S. K., Balasubramaniam, S. V., & Velluci, V. (2019). Sentinel-2/Landsat-8 product consistency and implications for monitoring aquatic systems. *Remote Sensing of Environment*, *220*, 19–29. https://doi.org/10.1016/j.rse.2018.10.027

Pahlevan, N., Sarkar, S., Franz, B. A., Balasubramanian, S. V., & He, J. (2017). Sentinel-2 MultiSpectral Instrument (MSI) data processing for aquatic science applications: demonstrations and validations. *Remote Sensing of Environment*, *201*, 47–56. https://doi.org/10.1016/j.rse.2017.08.033

Pahlevan, N., Schott, J. R., Franz, B. A., Zibordi, G., Markham, B., Bailey, S., et al. (2017). Landsat 8 remote sensing reflectance (Rrs) products: evaluations, intercomparisons, and enhancements. *Remote Sensing of Environment*, *190*, 289–301. https://doi.org/10.1016/j.rse.2016.12.030

Qiu, Z., Xiao, C., Perrie, W., Sun, D., Wang, S., Shen, H., et al. (2016). Using Landsat 8 data to estimate suspended particulate matter in the Yellow River estuary. *Journal of Geophysical Research: Oceans*, *122*, 276–290. https://doi.org/10.1002/2016JC012412

Ralston, D. K., Geyer, W. R., & Warner, J. C. (2012). Bathymetric controls on sediment transport in the Hudson River estuary: lateral asymmetry and frontal trapping. *Journal of Geophysical Research*, *117*, C10013. https://doi.org/10.1029/2012JC008124

Ross, L., & Sottolichio, A. (2016). Subtidal variability of sea level in a macrotidal and convergent estuary. *Continental Shelf Research*, *131*, 28–41. https://doi.org/10.1016/j.csr.2016.11.005

Saari, H. K., Schmidt, S., Castaing, P., Blanc, G., Sautour, B., Masson, O., & Cochran, J. K. (2010). The particulate 7Be/210Pbxs and 234Th/210Pbxs activity ratios as tracers for tidal-to-seasonal particle dynamics in the Gironde estuary (France): Implications for the budget of particle-associated contaminants. *Science of the Total Environment*, *408*(20), 4784–4794. https://doi.org/10.1016/j.scitotenv.2010.07.017

Schoellhamer, D. H. (2002). Variability of suspended sediment concentration at tidal to annual time scales in San Francisco Bay, USA. *Continental Shelf Research*, *22*, 1857–1866. https://doi.org/10.1016/S0278-4343(02)00042-0

Shi, W., Wand, M., & Jiang, L. (2011). Spring-neap tidal effects on satellite ocean color observations in the Bohai Sea, Yellow Sea and East China Sea. *Journal of Geophysical Research*, *116*, C12032. https://doi.org/10.1029/2011JC007234

SHOM (2016a), MNT topo-bathymetrique cotier à 20m de l'estuaire de la Gironde – Aval, Projet TANDEM, https://doi.org/10.17183/MNT_COTIER_GIRONDE_AVAL_TANDEM_20m_WGS84.

SHOM (2016b), MNT topo-bathymetrique cotier à 20m de l'estuaire de la Gironde – Amont, Projet TANDEM, https://doi.org/10.17183/MNT_COTIER_GIRONDE_AMONT_TANDEM_20m_WGS84.

Sottolichio, A., & Castaing, P. (1999). A synthesis on seasonal dynamics of highly-concentrated structures in the Cironde estuary. *Comptes Rendus de l'Académie des Sciences - Series IIA - Earth and Planetary Science*, *329*(11), 795–800. https://doi.org/10.1016/S1251-8050(00)88634-6

Sottolichio, A., Castaing, P., Etcheber, H., Maneux, E., Schmeltz, M., & Schmidt, S. (2011). Observations of suspended sediment dynamics in a highly turbid macrotidal estuary derived from continuous monitoring. *Journal of Coastal Research*, *64*(2), 1579–1583.

Sottolichio, A., Hanquiez, V., Perinotto, H., Sabouraud, L., & Weber, O. (2013). Evaluation of the recent morphological evolution of the Gironde estuary through the use of some preliminary synthetic indicators. *Journal of Coastal Research, SI*, *65*, 1224–1229. https://doi.org/10.2112/SI65-207.1

Sottolichio, A., Le Hir, P., & Castaing, P. (2000). Modeling mechanisms for the turbidity maximum stability in the Gironde estuary, France. *Proceedings in Marine Science*, *3*, 373–386. https://doi.org/10.1016/S1568-2692(00)80132-1

Talke, S. A., de Swart, H. E., & Schuttelaars, H. M. (2009). Feedback between residual circulations and sediment distribution in highly turbid estuaries: an analytical model. *Continental Shelf Research*, *29*, 119–135. https://doi.org/10.1016/j.csr.2007.09.002

Turner, A., & Millward, G. E. (2002). Suspended particles: their role in estuarine bio-geochemical cycles. *Estuarine, Coastal and Shelf Science*, *55*, 857–883. https://doi.org/10.1006/ecss.2002.1033

Uncles, R. J., Stephens, J. A., & Harris, C. (2006). Runoff and tidal influences on the estuarine turbidity maximum of a highly turbid system: the upper Humber and Ouse Estuary, UK. *Marine Geology*, *235*, 213–228. https://doi.org/10.1016/j.margeo.2006.10.015

Vanhellemont, Q., & Ruddick, K. (2015). Advantages of high quality SWIR bands for ocean colour processing: Examples from Landsat-8. *Remote Sensing of Environment*, *161*, 89–106. https://doi.org/10.1016/j.rse.2015.02.007

Vantrepotte, V., Loisel, H., Mélin, F., Desailly, D., & Duforêt-Gaurier, L. (2011). Global particulate matter pool temporal variability over the SeaWiFS period (1997-2007). *Geophysical Research Letters*, *38*, L02605. https://doi.org/10.1029/2010GL046167

Warren, M. A., Simis, S. G. H., Martinez-Vicente, V., Poser, K., Bresciani, M., Alikas, K., et al. (2019). Assessment of atmospheric correction algorithms for the Sentinel-2A Multispectral Imager over coastal and inland waters. *Remote Sensing of Environment*, *225*, 267–289. https://doi.org/10.1016/j.rse.2019.03.018

Wei, J., Lee, Z., Garcia, R., Zoffoli, L., Armstrong, R. A., Shang, Z., et al. (2018). An assessment of Landsat-8 atmospheric correction schemes and remote sensing reflectance products in coral reefs and coastal turbid waters. *Remote Sensing of Environment*, *215*, 18–32. https://doi.org/10.1016/j.rse.2018.05.033

Wu, P., Shen, H., Ai, T., & Liu, Y. (2013). Land-surface temperature retrieval at high spatial and temporal resolutions based on multi-sensor fusion. *International Journal of Digital Earth*, *6*, 113–133. https://doi.org/10.1080/17538947.2013.783131

Zhang, M., Dong, Q., Cui, T., Xue, C., & Zhang, S. (2014). Suspended sediment monitoring and assessment for Yellow River estuary from Landsat TM and ETM + imagery. *Remote Sensing of Environment*, *146*, 136–147. https://doi.org/10.1016/j.rse.2013.09.033

Zhu, Z., Wulder, M. A., Roy, D. P., Woodcock, C. E., Hansen, M. C., Radeloff, V. C., et al. (2019). Benefits of free and open Landsat data policy. *Remote Sensing of Environment*, *224*, 382–385. https://doi.org/10.1016/j.rse.2019.02.016